Autonomous University of Nuevo Leon

School of Mechanical and Electrical Engineering

Department of Electrical Engineering

Feature Extraction from Motor Imagery - EEG signals using O-splines

By

Erick Alejandro González Rodríguez

Thesis for the degree of

MASTER OF SCIENCE IN ELECTRICAL ENGINEERING

Autonomous University of Nuevo Leon

School of Mechanical and Electrical Engineering

Department of Electrical Engineering

Feature Extraction from Motor Imagery - EEG signals using O-splines

By

Erick Alejandro González Rodríguez

Thesis for the degree of

MASTER OF SCIENCE IN ELECTRICAL ENGINEERING

San Nicolás de los Garza, NL   February 2024

UNIVERSIDAD AUTÓNOMA DE NUEVO LEÓN
Facultad de Ingeniería Mecánica y Eléctrica
Posgrado

Los miembros del Comité de Evaluación de Tesis recomendamos que la Tesis "Feature Extraction from Motor Imagery EEG signals using O-splines", realizada por el estudiante Erick Alejandro González Rodríguez, con número de matrícula 1622456, sea aceptada para su defensa como requisito parcial para obtener el grado de Maestría en Ciencias de la Ingeniería Eléctrica.

El Comité de Evaluación de Tesis

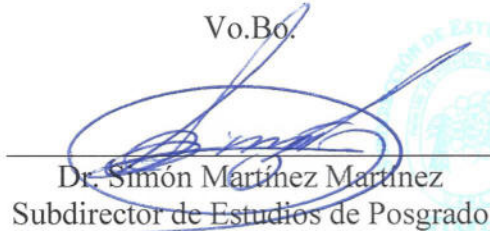Dr. José Antonio de la O Serna
Director

Dra. Luz María Alonso Valerdi
Co-director

Dr. José Ramón Rodríguez Cruz
Revisor

Dr. Jorge Aguilar Torrentera
Revisor

Dr. Johnny Rodríguez Maldonado
Revisor

Vo.Bo.

Dr. Simón Martínez Martínez
Subdirector de Estudios de Posgrado

Institución ____190001____

Programa __557520__

Acta Núm. __4311__

Ciudad Universitaria, a 16 de febrero de 2024.

This thesis is specially dedicated to…

My parents, for always making the greatest effort for us. For always showing support, and above all, for showing me how strong we are in the hardest moments. You both brought me into a life on which I am still looking my way, but with your help, every step I have made has been easier. Thank you.

My grandparents, for being a big cornerstone during my whole life. With you, I have laughed and learned about so many interests in different areas. Thank you for always showing me your love and care in all the distinct forms that you do.

A life without you would be hard. That is why I appreciate and thank you for every day you are close to me. I love you.

Acknowledgments

I would like to profoundly thank to several people who have been with me and have helped me before and during my time on this work.

Firstly, to the previous Neuroengineering and Neuroacoustics research group, currently the Nuero-Technologies research group, for opening me their doors to collaborate with them during the last three and a half years. Among them, to Dr. Luz María Alonso Valerdi and Dr. David Isaac Ibarra Zárate for their advice, lessons, and opportunities to provide useful things to both groups. To Norberto Naal, for being a great leader, guide, and a friend during all this time. And overall, to the current NeuroSense line of research: Kevin Cepeda, Angel Rivas, Vania Martínez, Fernanda Garibay and Sharon Hernandez, for demonstrating how much we can achieve when we do things together.

I thank my advisor, Dr. José A. de la O Serna, for his contribution to this work by explaining me the O-splines technique, discussing some results, and arriving to conclusions. At first, I was curious and interested (although, with not much knowledge) about the method and the signal processing field, and you have helped me understand the basis to make a better work.

To Dr. María Isolde Hedlefs Aguilar. There are many things I would like to thank you. You were the first person that guided me towards centering an idea of a genuine interest about a topic that I completely did not know, but that was fascinating to me. You taught me that one could comprehend every phenomenon by putting in the effort to investigate. With those bases, I have accomplished what I got in my time doing re-

search. Thank you for the work experience, but also for being an emotional support whenever it was necessary. Every conversation and advice derived in a large internal discussion that always concluded in the best decision against difficult situations. That has made me mature in some aspects. Thanks also for sharing meals and personal interests, which have always been enjoyable and interesting. Thank you for being a person that cares.

To Marifer Morones. For always showing me the kindness in people. For being a person that, although situations were difficult, always tries to stand still and to get through it. That is something to admire. Thank you for being with me during these years while doing the Masters, always supporting me, and making the workdays less complicated.

To my brothers, Diego and Iván, for the time at home where we could share games, preferences, and even thoughts. Whenever the days looked overwhelming, they always got better when I spend the time with you.

I also would like to thank to my friends: Julio Belmontes, Edgar Coronado, Gerardo Estrella, Kenya Vázquez and Dafne Chávez for their great confidence, time, and genuine interest in my work. Friends like you are difficult to find. Thank you for the conversations, amusing time, and for always being here.

A special thanks to FIME for the knowledge it provided me to obtain my engineer title, and now, to allow me to be part of the institution again, and develop this work for the master's degree.

Finally, I thank CONAHCYT for its support during the last two years of study in this Masters, on which I could develope this project, and that finishes with this thesis.

<div align="right">

Erick Alejandro González Rodríguez

February 2024

</div>

Abstract

Brain-Computer interfaces (BCIs) are systems that communicate the brain with external devices. To achieve this, electric cortical potentials go through a series of steps, such as their extraction, processing, and classification. Motor Imagination (MI) is an approach that induces cortical activity in the sensorimotor zone, which generates patterns of (de-)synchronization in the alpha (8-12 Hz) and beta (13-30 Hz) frequency bands during the preparation of movement. The processing of MI events entails a very important exercise for their correct classification, that is why the number of feature extraction techniques has seen a significant increase over the years.

Within this application, the O-splines, from the recently presented Discrete Taylor-Fourier Transform, are proposed as a technique capable of separating the frequency bands where MI events occur and extracting (de-)synchronization patterns. In addition, the O-splines allow estimations of parameters such as amplitude, phase, frequency, and rate of change of frequency, which provide richer information about brain dynamics. In this way, it is intended to use this modern technique to compare it with traditional quantification methods such as the estimations of event-related (de-)synchronization (ERD/ERS) patterns, as well as to describe the behavior of these events observing the characteristics that the method delivers.

Significant differences have been found when comparing against one traditional filtering technique ($p > 0.05$), and a higher classification accuracy was obtained against traditional ERD/ERS quantification technique. In addition, the O-splines state estima-

tion capacity extracted features that elevate the percentages of classification between two MI-classes to 92.31%.

Therefore, the O-splines could serve as a technique capable of extracting MI-patterns and classify between classes for BCI applications.

Contents

List of Figures

Nomenclature

AM   Amplitude Modulation

BCI   Brain-Computer Interface

CSP   Common Spatial Patterns

CWT   Continuous Wavelet Transform

DFT   Discrete Fourier Transform

DR   Distortion Rate

DTFT   Discrete Taylor-Fourier Transform

EEG   Electroencephalogram

EMD   Empirical Mode Decomposition

ERD   Event-Related Desynchronization

ERS   Event-Related Synchronization

FFT   Fast Fourier Transform

HT   Hilbert Transform

ICA   Independent Component Analysis

k-NN   k-nearest neighborhood

LDA   Linear Discriminant Analysis

LR   Logistic Regression

MI   Motor Imagery

PSD   Power Spectrum Density

RNA   Regularization Neighborhood Analysis

ROCOF   Rate of Change of Frequency

ROI   Region of Interest

SNR   Signal-to-Noise Ratio

SVM   Support Vector Machine

WT   Wavelet Transform

Chapter 1

Introduction

1.1 General Context

1.1.1 Brain-Computer Interfaces (BCI)

Brain-Computer Interfaces (BCIs) are complex systems independent from muscles and peripheral nerves that work as communication channels between the brain and external devices [5, 6]. The basic idea behind BCIs is to extract patterns/parameters from cortical activity related to specific internal or external events for converting them into control commands [7].

With this motivation, the research in BCIs has been growing exponentially since their first mention due to its extensive number of applications and the scope of developing non-invasive daily-life wearable BCIs [8, 6]. Most review papers name medical applications such as central nervous system assistance, rehabilitation, and mental disease detection as the most prominent applications [5, 9, 10]. Moreover, BCIs have also been developed in other fields like the construction of exoskeletons and robots [7, 5], environmental control from users [10, 6] and even gaming, art, or transport applications [10].

BCIs are normally composed of four important steps: (1) signal acquisition, (2) signal pre-processing, (3) feature extraction, and (4) feature classification [6]. Figure 1.1 shows graphically the whole BCI structure in which the two middle steps compose the **signal processing** process.
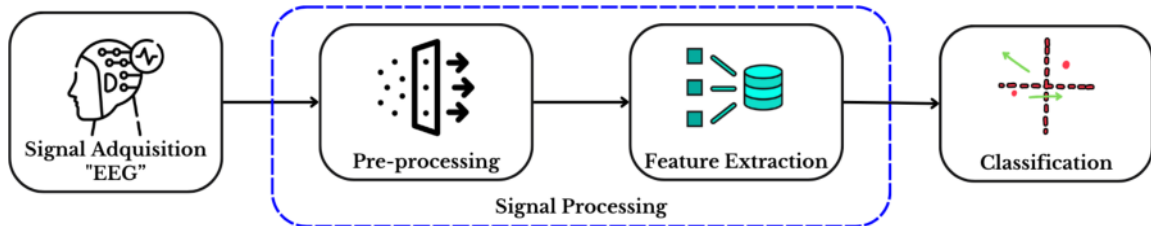
Figure 1.1: Brain-Computer Interfaces structure.

The first step uses different tools such as functional-Magnetic Resonance Imaging (f-MRI), Magnetoencephalogram (MEG), Positron Emission Tomography (PET), Transcranial Magnetic Stimulation (TMS) and Electroencephalography (EEG) for acquiring cortical signals [9]. For BCI applications, there is the need and goal to develop portable and non-invasive systems for using them in daily-life tasks and real-time activities for people in rehabilitation [6, 5]. In this matter, EEG has become the best choice that follows these specifications due to its high time resolution, portable characteristics, and low cost [9].

The signal processing step, where pre-processing and feature extraction are linked, is one of the most important along the whole BCI structure. Is in this one where the type of BCI is defined, and the one over which this work will be centered. The pre-processing step filters out all artifact related activity from the acquired signals to extract important features from clean data in the feature extraction step [8]. Furthermore, several reviews have separated the BCIs according to the proposed processing paradigms [7, 11, 12, 10], but in general, these can be differentiated between two types: evoked and spontaneous. The first ones are more reactive, while the second ones can be passive or active approaches. Figure 1.2 illustrates and mentions these, where the Motor Imagery
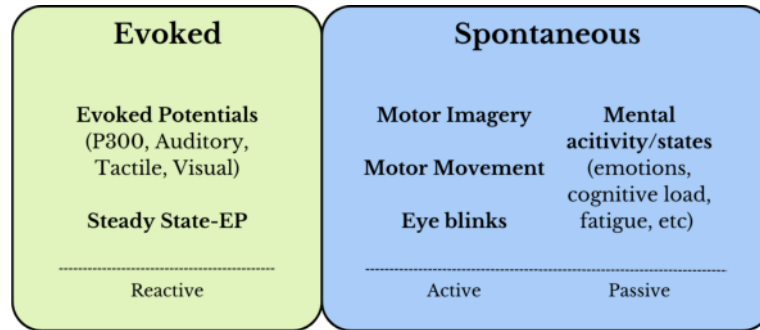
Figure 1.2: BCI different approaches.

approach will be the one over which this work will be focused.

Finally, the classification step uses Machine Learning, Neural Networks or even statistical based algorithms for detection and separation of patterns related to different classes [8]. Authors in [9] made an extensive review of methods for BCI applications, and named the Support Vector Machine (SVM), Random Forests (RF), Logistic Regression (LR), Liner-Discriminant Analysis (LDA) and Naïve-Bayes (NB) as the classification algorithms mostly used in BCI applications.

1.1.2 Motor Imagery (MI)

In [13], the author described the state of motor activity as three linked processes: action representation, motor intention and motor execution. With this idea, two notions could be raised: (1) the fact that exists a step before motor execution capable of visualizing the activity to be performed (preparation for future events), and (2) the idea that both steps (action representation and motor execution) could be separated by an actual intention of doing the intended action.

In 1979, authors in [14] investigated the called "rhythmic activity within the alpha band" as it appeared to be present in numerous other studies related to movement. There, it was described the presence of an energy desynchronization event moments before subjects made a movement, followed by a power recovery after the movement.

Later, in [1], both behaviors were discussed and described as event-related desynchronization (ERD) and synchronization (ERS). On one hand, ERD was defined as an attenuation of oscillations from the alpha (8-12 Hz) and beta (13-30 Hz) bands before motor activity, indicating preparation of movement. ERS, on the other hand, has been assumed to be related to an *idle* state where no activity is being processed, and was referred to a blocking state of cognitive processes or motor activity [1, 15]. Both events are shown graphically in an example in figure 1.3.
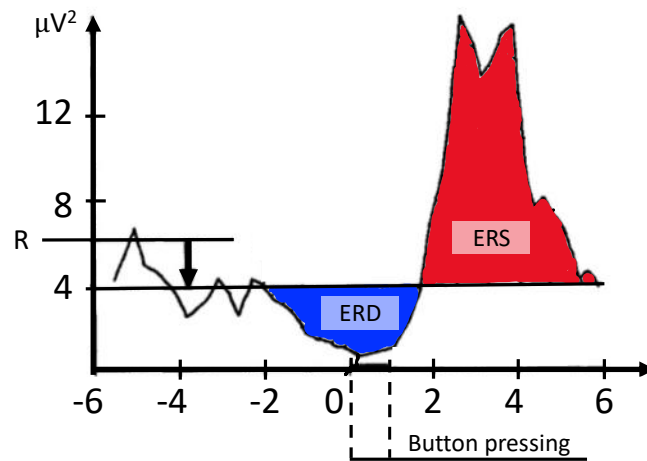
Figure 1.3: ERD and ERS events from a bipolar EEG recording (C3-Cz). The 0 second marks the button pressing in the paradigm, and R refers to the average alpha power at rest. Adapted from [1].

Although ERD/ERS patterns were first found when investigating motor activity, similar behavior was encountered in studies focused on the mental representation of the action [16]. This mental representation called **motor imagery (MI)** refers to the imagination of motor activity without performing the action, and derives into changes on physiological parameters such as heart and respiratory rates [17].

MI has been found to have differences in amplitude of the ERD pattern when is compared to the preparation of movement [17]. In one study [18], authors presented ERD patterns over the **primary sensorimotor area** contralateral to the hand perform-

ing the motor imagination, while ERS appeared ipsilaterally. This is, when the MI is done with the right hand, the ERD pattern was observed over the left hemisphere of the brain, while the ERS pattern was on the right hemisphere. Both cases on the same activation areas than movement preparation and mostly on both alpha and beta bands, something that was already declared before.

An example of this is the figure 1.4, which shows the scalp distribution of one subject's ERD/ERS pattern from the database used in this work. Note that the ERD pattern identified in blue is present contralaterally to the MI-class.
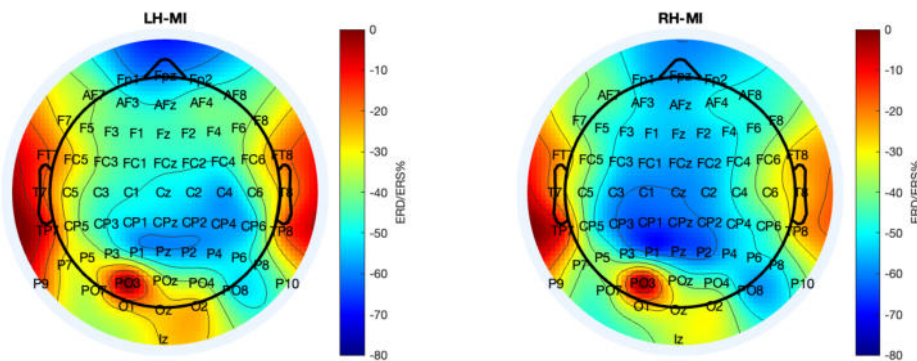
Figure 1.4: ERD/ERS scalp distribution example. Subject 14 from database [2]. ERD/ERS were calculated using the classical power approach described in [3]. Signals were band-pass filtered in 8-12 Hz.

In recent years, other contributions to the MI understanding have been given. For example, authors in [19] measured connectivity of brain areas before (pre), during (para) and after (post) the MI event, finding strong connections on the occipital cortex during pre-MI, contralateral sensorimotor cortex on para-MI, and symmetrical connections between occipital and sensorimotor areas during post-MI. In [20], authors found similar connectivity during MI and motor execution, and described more connections on right-hand than left-hand MI due to that all (elderly) subjects were right-handed in the study. And finally, another study [21] visualized more segregation and transitivity over the alpha band (instead of beta band) while going from the pre-MI state to the para-MI

one, as well as more power desynchronization lateralization during the MI-event.

At the end, with all this information, the importance of developing techniques capable of extracting MI features for MI-based BCIs has grown. And, with this goal, many works have proposed new methods for separating different number of MI classes.

1.2 Related Works

Signal processing in MI has been a topic of great focus in recent years. Different kind of signal processing techniques have been proposed for MI feature extraction. Applications in robots and prosthesis have marked a pathway in which the best proposed method should overcome artifacts and low signal-to-noise ratio to accomplish high classification rates between different MI-classes.

Numerous studies have delivered new and benchmarking techniques during the years. Table 1.1 summarizes recent works with their proposed techniques and some of their respective results.

Table 1.1: Recent state-of-the-art techniques proposed for extracting MI features.

First part of Table 1.1.			
Type	**Proposed Technique**	**Year**	**Results (best)**
ERD/ERS	AM: Hilbert Transform Power	2020 [22] 2023 [23] 2021 [24]	ACC= 86.11% and 83.24%. ACC= 86.11%, 78.74%, 74.73%. ERD/ERS (%): CP2=-9.8, CP1=-8.8, C4=-8.3 and Cz=-7.1
	Lock-in Amplifier (LIA)	2018 [25]	Maximal Correlation Coefficient (MCC) = 0.86 and Time delay = 210ms.

<div align="center">Continuation of Table 1.1.</div>

Type	Proposed Technique	Year	Results (best)
CSP	Sub-band CSP + Sequential Backward Floating Selection	2019 [26]	ACC=86.5% in average.
	CSP, FBCSP and FBC-SSP	2022 [27]	FBCSP=75.11%, FBCSSP=70.5% and FBCSP=75.01% FBC-SSP=76.3%.
	Separable Common Spatio-Spectral Patterns (SCSSP)	2016 [28]	Cross-validation ACC: Exp1=62,34% and Kappa Coef.: Exp2=42.17.
	Sparse Time-Frequency Segment CSP	2016 [29]	ACC= ~90.4% in avg.
	CSP+Neighborhood Component Analysis (NCA)	2020 [30]	ACC=~93% in avg.
	FB Regularized-CSP + Mutual Information Based Individual Feature	2018 [31]	ACC=86.23% in avg.
	Improved-CSP: Bhattacharyya distance	2019 [32]	ACC=91.25% and 90.43%.
WT	Wavelet-based Temporal-Spectral-Attention Correlation Coefficient	2023 [33]	ACC in avg: Data1=81.45%, Data2=81.78% and Data3=83.31%.

Type	Proposed Technique	Year	Results (best)
	DWT+Reimannian Graph+Regularization	2021 [34]	ACC in avg: Data1=~ 88% and Data2=83.31%
	Pearson Correlation Coefficient (PCC)+DWT	2023 [35]	ACC in avg: SVM=90.88% and kNN=90.10%.
	Flexible-Analytic WT (FAWT)	2020 [36]	ACC in avg=85.26%.
	Dual-Tree Complex WT+NCA+CSP	2021 [37]	ACC in avg: Data1=84.02% and Data2=89.1%.
	Harmony Search	2020 [38]	ACC in avg=93.61%.
FT	Bispectrum+CSP	2020 [39]	ACC in avg: Data1=83.8%, Data2=86.3% and Data3=77.8%.
	FFT	2018 [40]	ACC (2 approaches): FFT1 (8-32Hz)=58% and FFT2 (3 bands)=59%.
Others	Ensemble-EMD	2023 [41]	ACC: Bagged Ensembled=96.17%.
	DWT+SPR+CSP	2023 [42]	ACC: Data1=98.83% and Data2=92.16%.
	ICA+WT	2022 [43]	SNR: Channels FPz, F3, Fz and F4 > 20.
		2021 [44]	ACC in avg: kNN=98.88%, SVM=94.33% and RF=99.44%.

From Table 1.1, it is to highlight the great use of the traditional and always func-

tional ERD/ERS quantification method. The Common Spatial Patterns (CSP), which has become the gold-standard in MI-BCI applications, is also worth mentioned, as well as the popular Wavelet Transform (WT).

Regarding the first, it quantifies the amplitude variations in time from the power of the frequency band in observation after a period of reference [3]. Moreover, two different approaches have been used over the years for this quantification technique: the power variation approach [3] and the amplitude modulation one [4]. The first squares the samples to obtain power values and the second extracts the complex envelope of a band-pass signal for amplitude measurement. More of this last approach on the next chapter (subsection 2.1.1).

The widely used CSP is a technique capable of separating spatially until two different classes of events by maximizing the variance of one class from a spatial patterns' matrix [45]. Its introduction in [46] set a precedent in the MI signal processing analysis due to the incorporation of spatial filters into the temporal analysis. From here, diverse variations have been trying to find the most suitable missing piece in the technique for increasing the classification performances, as can be seen on Table 1.1.

Wavelets, on the other hand, have been a popular method in EEG analysis due to their dynamic time-frequency resolution. Works have used the WT as a pre-processing step [44], complex features extraction [34, 33] and even to quantify the ERD/ERS pattern [25]. Its applicability in EEG signals and (especially) MI works drove the authors in [47] to compare different bases, finding the best capacities in the **rbio2.2** mother wavelet.

Outside these normally used methods, other studies have proposed spectral based techniques. Authors in [48] used an Auto-Regressive (AR) technique for online evaluation due to its high quality of amplitude estimation in short periods of time, which is defined by the model order normally between 3 and 20 [49]. Empirical Mode Decomposition (EMD) has also been used widely with its own variations. For example, the

Multivariate-EMD proposed in [50] with CSP obtained 79.19% and 79.18% in classifying between two MI-classes using LDA and SVM classifiers, respectively. Besides, [51] used Multivariate-EMD with the Hilbert Transform (HT) for calculating synchronization between electrodes before and during the MI task.

Some works focus their analysis on the pre-processing step. In [52], authors used Independent Component Analysis (ICA) for explaining relations and activation zones between motor-imagination, motor-observation, and motor-execution. In another study [43], authors combined ICA with the WT for de-noising the signal before entering the CSP method, having higher SNR values (> 20) than using only ICA (< 20), and relatively high mean average accuracies with different classifiers (>75%).

Some other works look for reducing characteristics and take only the ones that are most related to MI activity. Instead of using all EEG channels for analysis, author in [35] proposed to use Pearson Correlation Coefficient (PCC) to find the most significant channels to MI activity, which led to classification accuracies of 90.88% and 90.10% using SVM and k-nearest neighborhood (k-NN) classifiers, respectively. Modhiwale and colleagues [38] used the "harmony search" optimization algorithm for extracting only the best spectral and temporal-spectral characteristics after the Discrete WT (DWT), delivering 92.49% of accuracy using k-NN.

Finally, other studies combined different methods. For instance, authors in [42] proposed to use a graphic technique to obtain energy changes from one same point, and combined the technique with the DWT and CSP for obtaining high classification percentages (>90%). In [37], the Dual-Tree Complex Wavelet Transform is presented with CSP and Regularization Neighborhood Analysis (RNA), and had accuracies higher than 80%. Also, in [39], CSP was used after obtaining the spectrum of the signal with the Fourier Transform (FT), delivering the highest classification accuracy of 86.3%.

Certainly, most of the aforementioned methods accomplished the goal of obtaining great classification accuracies. But this must coexist with several other considerations

for applying into real-time BCIs approaches.

1.3 Problem Statement

Although, many techniques have proven to be efficient for characterizing MI activity in different domains and accomplished high classification performances for identifying different MI-classes, other characteristics and considerations are forgotten.

On one hand, to extract the best features for classification, the signal must pass for (and, therefore, rely on) a pre-processing step. EEG signals are composed of either endogenous (interior sources) or exogenous (exterior sources) kind of noises, normally called **artifacts** [6]. They also have the characteristic of being non-stationary with small variations in time due to cognitive activity [9]. Then, is not surprising to see the amount of works focusing on the pre-processing step [43, 44, 37, 53] to obtain only the necessary information from the original data.

From [9], it can be inferred that the band-pass filters (especially Butterworth filters) are the most used in different investigations using EEG signals for extracting frequency bands of interest. But some parameters must be set before designing these and other type of filters.

In applications regarding Event-Related Potentials (ERPs), Widmann and colleagues [54] proposed to use filters with stop-band attenuation gains around **-54 and -60 dB**. But, in general, to attenuate major artifact activity, it is required the right tuning of the filters. Parameters like the filter type, cut-off frequency, pass-band ripple, or roll-off have to be defined carefully by also considering the nature of the signal. On the contrary, bad design of filters could lead into different affectations on the signal such as spurious oscillations, delays, loss of information or temporal blurring [55]. Thus, several considerations have to be well thought before designing filters, which is time consuming and could also take more execution time while analyzing signals.

On the other hand, most of the works extract amplitude related features for classification. The first presentation of the ERD/ERS method for capturing the amplitude power changes during MI event drove to the high utilization of these characteristics. Consequently, proposed techniques use to work with power [23], time-frequency energy resolution [33] and even spatial amplitude changes [25], but limited number of studies focus their investigation on other physical and temporal features.

In this matter, the **phase** has been accepted as relevant feature in EEG signals due to its capacity to measure changes in synchrony [56] and having better properties than amplitude [56, 57]. Although, works that have worked with this parameter showed regular classification rates. Authors in [58] showed accuracies of 61.7% and 61.9% when identifying two classes of MI-activity from the same limb while using the Phase-Locking Value (PLV) calculated from the **instantaneous phase**. Also, Benzy and Vinod [59] delivered an average accuracy (n=12) of 63.7%. These results changed when using amplitude and phase features together, which has been reported to rise the classification accuracies to higher than 80% [34].

In this matter, a proposition is to use techniques that can extract, not only amplitude and energy features, but also the phase and derivates of phase, in a way that they explain the dynamics behind MI-activity and get useful values for BCI applications.

1.4   Proposed Method

After reviewing a few of the problems in MI signal processing, it was important to consider tools capable of overcoming the presented limitations. With this in mind, this work introduces the O-splines into the MI-BCI applications.

The O-splines come from the low-pass differentiators of the expansion of the Discrete Fourier Transform (DFT) called the **Discrete Taylor-Fourier Transform (DTFT)** [60]. In general, this method adds Taylor terms of the Taylor Series to the Fourier co-

efficients, which expands the Fourier basis to a Taylor-Fourier one [60]. Consequently, it overcomes the FT periodic signal assumption, and two of its most important limitations: (1) spectral leakage and (2) harmonic interference [61].

This technique can be illustrated as FIR filters with maximal flat gains, which work as ideal band-pass filters modulated to a central frequency [62]. These characteristics result in less distortion and harmonic interference [61]. Figure 1.5 shows the impulse and frequency responses from the 9-th order O-spline.
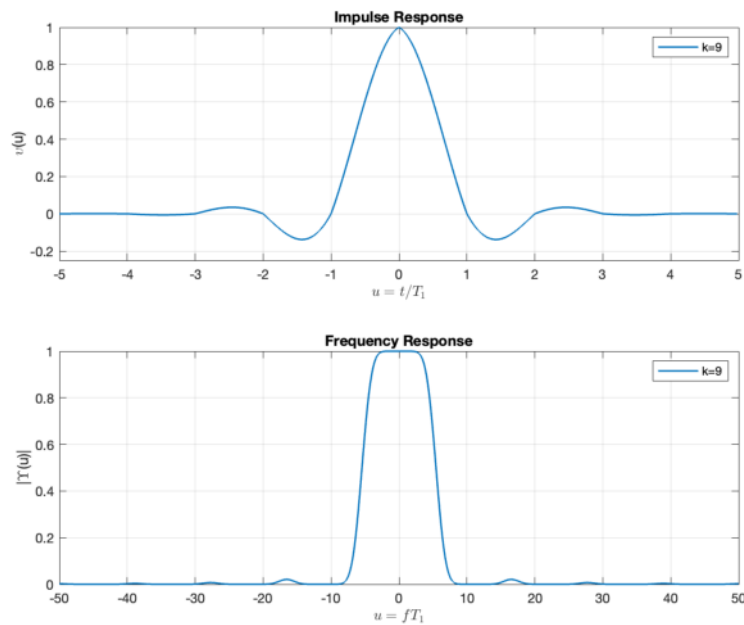
Figure 1.5: Graphic responses from the O-spline of order 9.

Furthermore, the low-pass differentiators from the DTFT allow **state estimations** from the signal input [61]. This is, the O-splines deliver not only estimates of amplitude and phase, but also, their consecutive derivatives, estimating other parameters such as amplitude derivations, frequency, and the rate of change of frequency (ROCOF). This capacity has led authors to performed analysis in different fields like power systems and bio-signals. The table 1.2 resumes some works where the O-splines have been applied.

Essentially, the O-splines started in the power systems area by analyzing oscillating

Table 1.2: Previous works using the O-splines technique.

Field	Year	Description
Power Systems	2018 [60]	Power oscillating signal analysis.
	2020 [63]	Synchrophasor estimations.
	2020 [64]	Detection of faults.
	2023 [65]	Inertia estimations using wide-area monitoring systems (WAMS) in power grids.
Biosignals	2013 [66]	Separation of breathing and cardiac rhythms from blood pressure signals.
	2018 [67]	Detection of ventricular arrhythmia in EKG.
	2020 [62]	Frequency-band extraction of epilepsy EEG signals.

voltage and current signals and comparing results with standard measurement equipment. However, in recent years, the number of works applying the O-splines in biosignals has been increasing, and this work will follow this direction by applying this technique into the MI-signal analysis.

1.4.1 Why the O-splines? (Justification)

The proposed O-splines have some characteristics worth mention for entering MI signal analysis.

In the first place, their FIR filter natural form can separate harmonics from the central frequency in analysis. In [68], it was reported the high attenuation gains of the O-splines while increasing its order. At the order nine, the attenuation gains went from **-47dB to -326dB**, which makes it more appropriate in comparison to the gains recommended in [54].

In its only EEG-signals-related study [62], the O-splines could effectively extract the different frequency rhythms over which the brain works. Specifically in MI-EEG signals, it has been reported and stated that the range of the frequency band of interest covers the **alpha** and **beta** bands [18]. Therefore, with this previous knowledge, the O-splines filtering capacity could separate the bands in question in a way that other harmonics

do not interfere in the output signal.

Furthermore, the O-splines have the capacity to extract features due to their low-pass differentiators. A point to highlight from this is the relevance and physical meaning these features have. Other popular and majorly used techniques deliver pertinent information from the signal, but this not normally have physical meaning. For instance, the WT is a technique capable of filtering and giving a dynamic time-frequency resolution, but their coefficients do not have physical meaning [61], and the correct choose of mother wavelet derives into tedious high calculus operations (as described in [9]) and even a complete research work for identifying the most suitable one for specific applications [47].

In a comparative work, author in [69] uses CSP features, spectral features (the PSD) and Hjorth temporal parameters. These lasts referring to signal power, frequency, and changes in frequency. As result, the classification percentages were higher with temporal features than with the gold-standard spatial ones for segregating between two (93.6%), three (70.3 %) and four (58.3%) classes of MI. This would imply a better performance when using temporal derivatives of the parameters, and the O-splines can give not only amplitude and phase features, but derivatives with physical meaning [63].

Finally, other studies have used the O-splines in bio-signals, although none of them have proposed the technique into MI-EEG signal applications. Therefore, the O-splines' features are themselves a contribution into the field of MI-EEG signal analysis.

1.5 Research Questions

With this proposition, a few questions raised.

- Can the O-splines extract better MI patterns than traditional approaches?

- Can the O-splines filtering capacity extract only the energy of both alpha (8-12

Hz) and lower-beta (13-14 Hz) combined (8-14 Hz)?

- Are the O-splines capable of characterize amplitude, phase, and frequency variations over the band of interest in MI events?

1.6 Hypothesis

Knowing the O-spines capacity, three hypotheses were set.

- The O-splines will filter artifact sources from the EEG signal, which will result in a visually more defined ERD/ERS pattern against traditional approaches.

- The O-splines will extract only the energy of alpha (8-12 Hz) and low-beta (13-14 Hz) bands combined (8-14 Hz) with non-harmonic interference.

- The O-splines' state estimation capacity will characterize changes on all features (amplitude, phase, frequency, and ROCOF) during the MI-event.

1.7 Objectives

Finally, to answer the research questions and proof the hypotheses, the next goals were defined.

1.7.1 Main Goal

To validate the O-splines technique as a tool capable of extracting Motor Imagery event features from EEG signals.

1.7.2 Particular Goals

1. To quantify event-related (de-)synchronization for comparison between traditional ERD/ERS method against the O-splines technique.

2. To extract alpha and lower-beta bands combined information related to the Motor Imagery ERD using the O-splines filtering capacity.

3. To use the O-splines as an estimation tool for amplitude, phase, frequency, and ROCOF on Motor Imagery events for characterization of their responses.

Essentially, this thesis has the goal of introducing in a detailed way the work done during the research. Its structure began in this chapter with the introduction of the MI-BCI concept, the state-of-the-art methods for extracting MI characteristics, the problems on these methods, the proposition made for the work, hypotheses, questions, and objectives.

It follows in Chapter 2, which contains a short review with of some of the models mostly used in MI-EEG analysis. Characteristics and limitations of these models are described (section 2.1), as well as the traditional approach to be compared against the proposed technique (subsection 2.1.1). In addition, in section 2.2 the DFT is explained as the method over which the **DTFT** was developed. In section 2.3 concepts behind O-splines modeling, such as Dynamic Phasor (subsection 2.3.1), Digital Taylor-Fourier Subspace (2.3.2) and impulse and frequency responses (2.3.3) are presented. Finally, the designed O-spline models for this work are shown in subsection 2.3.4.

Next, the Chapter 3 explains the steps followed for extracting MI-EEG signal parameters such as ERD/ERS patterns and state estimations ones. In section 3.1, the MI-EEG signals database used in this work is described. Section 3.2 resumes both tasks marked for the present work: at subsection 3.2.1, the ERD/ERS quantification process is described using traditional ERD/ERS: AM and the novel O-splines technique, and in sub-

section 3.2.2 the state analysis using the O-splines' estimation capacity. The statistical tests utilized to infer data behavior are mentioned in subsection 3.2.3. And finally, subsection 3.2.4 describes the classification models used in an extra step to measure the performance of the proposed technique.

In Chapter 4, the results of the tasks defined for this work are shown. The chapter is divided in several sections: the temporal ERD/ERS analysis (section 4.1) with a comparison between the filters used (subsection 4.1.1), state estimations with O-splines (4.2), and classification accuracies (4.3). Also, with the same structure, the Chapter 5 discusses the previous findings, and comments about the future directions and limitations of the work. Lastly, the Chapter 6 concludes this work with a short recap of the results.

Chapter 2

Theoretical Framework

In this chapter, it is expected to understand important points of some of the models that have been served as basis for other state-of-the-art techniques. So, at the end, it is understandable the choose of using the traditional ERD/ERS approach. In addition, the O-splines' mathematics are also described by explaining a few of the concepts behind them, so the technique can be comprehended before using it.

2.1   Models

The previous state-of-the-art methods have one characteristic in common, that the majority of them proceed from the basis of a technique introduced before, e.g. the CSP, WT or the FT. In table 2.1 some of the characteristics and limitations of these techniques are described.

Table 2.1: Characteristics and limitations from the basis methods.

First part of Table 2.1.		
Method	**Characteristics**	**Limitations**
ERD/ERS [3, 70]	• Quantifies the percentage of change of energy from the frequency band of study. • Time-locked but not phase-locked. • Can be extracted by temporal methods or time-frequency ones.	• Limited to only the temporal domain. • Loss of information by averaging over time.
CSP [49, 12, 71]	• Includes frequency and spatial filters. • Minimizes and maximizes the variances between two classes of activities. • Performs multichannel analysis.	• Depends on the frequency band of analysis. • Discards temporal information. • Limited to segregate between two classes of tasks.

Method	Characteristics	Limitations
	Continuation of Table 2.1.	
WT [9, 12]	• Gives a balanced time-frequency resolution: wide windows on the lower frequencies and narrow on the higher ones. • Decomposes the signal with a series of low-pass and high-pass filters. • Each decomposition has its coefficients, maintaining the temporal information.	• Choosing the right mother wavelet for one specific task represents a challenge before analysis. • Oscillations, shift variance, aliasing and lack of directionality are considered as other limitations of the method [72].
FT [9, 49]	• Estimates the frequency representation of a signal. • Captures, in high resolution, the different frequency components from a signal. • Works better with stationary signals.	• No temporal resolution. • Not suitable for non-stationary signals.

	Continuation of Table 2.1.	
Method	**Characteristics**	**Limitations**
EMD [9, 41]	• Decomposes the signal into Intrinsic Mode Functions (IMFs) where time-frequency information is kept as sub-signals. • Data-driven method. • Suitable for non-stationary signals.	• Does not overcome inter-channel interference. • Mode-mixing: information from the same frequencies can be found on different IMFs. • Might remove redundant information or eliminate pertinent one.

Note in the table the differences among the methods. The ERD/ERS traditional approach is limited to the analysis in the temporal domain and captures the events in specific time lapses. In contrast, the FT captures only the spectral information of one raw signal, although it works better for non-dynamic signals. EMD and WT combine both informations to assure a better decomposition of the time signal inside different frequency bands. The former adapts to the data but allows the presence of other frequency information into the decomposition modes. While the last uses a set of filters in the analysis, even though is challenging to define the best mother wavelet. Finally, CSP uses spatial information to manage the data of the most active channels, however the temporal information is lost.

In MI analysis, is important to extract information at the time when the event appears. Therefore, in this work the ERD/ERS: AM approach is considered as the method

to be compared against the O-splines. This is due to its capacity to capture important amplitude changes in the temporal domain, and because of its importance and impact for explaining both ERD and ERS in MI.

2.1.1 ERD/ERS: AM

The ERD/ERS amplitude modulation (AM) approach involves the introduction of traditional telecommunication analysis into the ERD/ERS quantification task, as it delivers better time resolution than the classical power approach [4]. ERD/ERS: AM starts with the band-pass filtering of the signal (1), then a complex envelope is given to the band-pass signal by means of the HT (2), and finally the averaging of the envelopes obtained for all trials (3) [3].

The main operation of this approach is performed under the first two previous steps. The signal must be filtered first to assure that the operation is performed only over the frequency band of interest. Furthermore, filters will also generate a band-pass representation of the signal, which is real and positioned far from the 0 frequency [73].

The HT is used in the second step, and it is defined by equation 2.1.

$$H[x(t)] = \widehat{x}(t) = \frac{1}{\pi} \int_{-\infty}^{\infty} \frac{x(\tau)}{t - \tau} d\tau \tag{2.1}$$

This notation indicates a shift in the phase from the original signal by $-\pi/2$, and forms the **analytic signal** of the equation 2.2.

$$X(t) = x(t) + j\widehat{x}(t), \tag{2.2}$$

where x(t) is the real part of the complex signal, and the imaginary refers to its HT. With this notation, pertinent information from the instantaneous amplitude, phase and even frequency can be obtained [74].
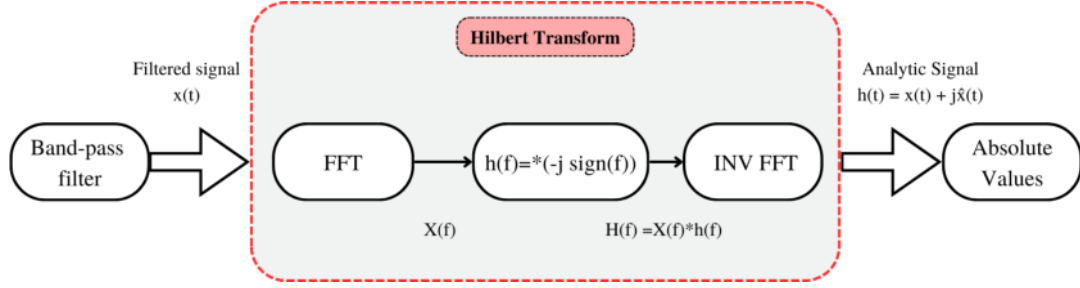
Figure 2.1: ERD/ERS: AM approach in this work. Figure based on the one in [4].

In the case of the analysis in this work, the absolute values are obtained from the analytic signal to measure the amplitude changes in the envelope. The figure 2.1 shows a short diagram of these steps before going through trials segmentation and trials averaging. Note that the HT is defined by using the Fast Fourier Transform (FFT) spectral transformation.

2.2 Discrete Fourier Transform

Having N consecutive samples from a signal $x[n]$ in the range $0 \leq n \leq N-1$ of a periodic or an aperiodic sequence, the *Discrete Fourier Transform (DFT)* of a N-point is

$$X[k] \triangleq \sum_{n=0}^{N-1} x[n] e^{-j \frac{2\pi}{N} kn}, \qquad 0 \leq k \leq N-1, \tag{2.3}$$

where the index k corresponds to a discrete set of frequencies defined by $w_k = \frac{2\pi}{N}$, $k = 0, 1, ..., N-1$. Moreover, the DFT can be reversed by using its inverse version, the *Inverse Discrete Fourier Transform (IDFT)*. It allows to recover the original signal sequence from the previous frequency coefficients [75]. For any N coefficients $X[k]$, $0 \leq k \leq N-1$, N samples values are calculated using

$$x[n] = \frac{1}{N} \sum_{k=0}^{N-1} X[k] e^{j \frac{2\pi}{N} kn}. \tag{2.4}$$

This pair of equations are denoted as $x[n] \leftrightarrow X[k]$.

Normally, the exponential part of the definition of the DFT in equations 2.3 and 2.4 is defined with the well-known *twiddle factor w_N*,

$$w_N = e^{-j\frac{2\pi}{N}}. \tag{2.5}$$

So, the DFT **analysis equation** can be written in matrix form as

$$X = W_N \cdot x, \qquad X = \begin{pmatrix} X[0] \\ X[1] \\ \vdots \\ X[N-1] \end{pmatrix} \tag{2.6}$$

and the **synthesis equation** as

$$x = \frac{1}{N}(W_N^* \cdot X), \qquad x = \begin{pmatrix} x[0] \\ x[1] \\ \vdots \\ x[N-1] \end{pmatrix} \tag{2.7}$$

where W_N^* is the complex conjugate of the Fourier matrix W_N which has the form

$$W_N = \begin{pmatrix} 1 & 1 & 1 & \dots & 1 \\ 1 & w_N & w_N^2 & \dots & w_N^{(N-1)} \\ 1 & w_N^2 & w_N^4 & \dots & w_N^{2(N-1)} \\ \vdots & \vdots & \vdots & \ddots & \vdots \\ 1 & w_N^{(N-1)} & w_N^{2(N-1)} & \dots & w_N^{(N-1)^2} \end{pmatrix}, \tag{2.8}$$

which is an important component in the DTFT.

2.3 O-splines Modeling

The idea behind the O-splines and the DTFT was developed over the concept of the dynamic phasor from power systems [76]. It consists of the approximation of a Taylor polynomial to the complex envelope of a band-pass signal [76][61].

2.3.1 Dynamic Phasor

An ideal model for the dynamics of a band-pass signal is the one shown in equation 2.9,

$$s(t) = a(t)\cos(2\pi f_1 t + \varphi(t)), \tag{2.9}$$

where $a(t)$ and $\varphi(t)$ correspond to the varying-in-time amplitude and phase, respectively, being f_1 the fundamental frequency of the signal. By rewriting 2.9 into a complex function, it gets the equation 2.10,

$$s(t) = \Re\{\xi(t)e^{j2\pi f_1 t}\}, \tag{2.10}$$

which the $\xi(t)$ component is the complex envelope (or dynamic phasor) and can be written in polar form as $\xi(t) = a(t)e^{j\varphi(t)}$.

The inclusion of Taylor terms to the signal model expands and approximates the signal by inserting a k-th order Taylor polynomial at $t_0 = 0$. Although, this can only be possible, if and only if, the dynamic phasor is given by an analytic equation. The general form of the Taylor polynomial is given by equation 2.11, where its coefficients are progressive derivatives at the interval center.

$$\xi_k(t) = \xi(t_0) + \xi'(t_0)t + \xi''(t_0)\frac{t^2}{2!} + ... + \xi^k(t_0)\frac{t^k}{k!}, \qquad \frac{-T}{2} \le t \le \frac{T}{2}. \tag{2.11}$$

2.3.2 Digital Taylor-Fourier Subspace

When the dynamic phasor concept first appeared in [76], it was implemented with a set of third order FIR filters. In the work, the set of filters with constant, linear, and quadratic gains, allowed a more suitable and low-error estimation of amplitude and phase of an oscillatory signal.

Moreover, its presentation led to the addition of Taylor polynomials to the FT in [61] for dealing with the steady-state limitation of the FFT. As result of this, the Fourier subspace was then expanded to a Taylor-Fourier one [60]. In other words, the DTFT spans the space up to the k-th Taylor term, while the FFT spans only the Fourier space referred to the zero-th Taylor term.

The extension of the Taylor-Fourier subspace begins with the presentation of the Fourier synthesis equation, which is

$$x = W_N \xi, \tag{2.12}$$

where the $N \times N$ matrix W_N is the Fourier matrix, and the vector ξ contains the Fourier coefficients of a periodic sequence. The elements of the Fourier matrix are defined by the twiddle factor w_N in equation 2.13, which has $w_N^{nk} = e^{j\frac{2\pi}{N}}$ for $n,k=0,1,\ldots,N\text{-}1$ as elements, being N the samples per cycle.

$$W_N = \begin{pmatrix} 1 & 1 & 1 & \ldots & 1 \\ 1 & w_N & w_N^2 & \ldots & w_N^{(N-1)} \\ 1 & w_N^2 & w_N^4 & \ldots & w_N^{2(N-1)} \\ \vdots & \vdots & \vdots & \ddots & \vdots \\ 1 & w_N^{(N-1)} & w_N^{2(N-1)} & \ldots & w_N^{(N-1)^2} \end{pmatrix} \tag{2.13}$$

In consequence, the Fourier analysis equation is

$$\widehat{\xi} = W_N^{-1} x = \frac{1}{N} W_N^H x. \tag{2.14}$$

Following the description in [60], by including more and more Taylor terms, the model gets more general, resulting in the form of equation 2.15,

$$x = \Phi_k \xi_k, \tag{2.15}$$

where

$$\Phi_k = \left(1 \begin{pmatrix} W_N \\ W_N \\ \vdots \\ W_N \end{pmatrix} \quad T \begin{pmatrix} W_N \\ W_N \\ \vdots \\ W_N \end{pmatrix} \quad \cdots \quad \frac{1}{k!} T^k \begin{pmatrix} W_N \\ W_N \\ \vdots \\ W_N \end{pmatrix} \right) \qquad and \qquad \xi_k = \begin{pmatrix} \xi_N \\ \dot{\xi}_N \\ \vdots \\ \xi_N^{(k)} \end{pmatrix},$$

in which $\frac{1}{k!} T^k$ are diagonal matrices containing the successive Taylor terms and their derivatives; Φ_k is $(k+1)N \times (k+1)N$ of dimensions and contains the expanded subspace basis. Meanwhile, the subvector ξ_N has the k-th order Taylor-Fourier coefficients and the rest, $\xi_N^{(k)}$ for $k=1,2,\ldots,k$, their successive derivatives. In this matter, one can observe the implication of the cyclic extension introduced by the order of the Taylor polynomial expansion defined as $C=k+1$.

However, the addition of the Taylor terms removes the orthogonality of the vector from the Fourier model. Therefore, for orders $k > 0$, there is the need of a pair of biorthonormal bases to accomplish orthogonal projection [60]. This necessity derives in the dual form (analysis equation) of equation 2.15, which is

$$\widehat{\xi} = \Phi_k^{-1} x. \tag{2.16}$$

Since base vectors in Φ are not orthogonal, the biorthogonal basis (the o-splines and derivatives) is found in the vectors of the dual matrix $\widehat{\Phi}_k$ of Φ_k, which is

$$\widehat{\Phi}_k = \Phi_k^{-H}, \tag{2.17}$$

such that $\Phi_k^H \Phi_k = I$.

Then, in terms of the dual matrix, we have

$$\widehat{\xi} = \widehat{\Phi}^H x. \tag{2.18}$$

The Fourier matrix in 2.15 can be factorized in cyclic submatrices,

$$\Phi_k = \Upsilon_k \Omega_k$$

$$\Phi_k = \begin{pmatrix} 1 & T_1 & \dots & \frac{1}{k!}T_1^k \\ 1 & T_2 & \dots & \frac{1}{k!}T_2^k \\ \vdots & \vdots & \ddots & \vdots \\ 1 & T_C & \dots & \frac{1}{k!}T_C^k \end{pmatrix} \begin{pmatrix} W_N & 0 & \dots & 0 \\ 0 & W_N & \dots & 0 \\ \vdots & \vdots & \ddots & \vdots \\ 0 & 0 & \dots & W_N \end{pmatrix}, \tag{2.19}$$

where T_i for $i=1,2,\dots,C$, are $N \times N$ diagonal matrices with cyclic segments of the k-th order Taylor term. The factorization separates the Taylor-Fourier component Φ_k into the Taylor (Υ_k) and the Fourier (Ω_k) operators with the great advantage that elements in Υ_k are real and FFT can be used for modulations due to matrix Ω_k.

The former factorization was proposed in the study [66] for reducing computational cost and for simplifying the dual form into equation 2.20,

$$\widehat{\Phi} = \Upsilon(\Upsilon^H \Upsilon)^{-1} \frac{\Omega}{N} = \widehat{\Upsilon} \frac{\Omega}{N}. \tag{2.20}$$

The formulation was presented in [60] with the idea of designing low-pass filters with maximally flat low-pass differentiators in $\widehat{\Upsilon}$. Thus, vectors from $\widehat{\Phi}$ are harmonic

modulations out of the $\widehat{\Upsilon}$ vectors at the harmonic frequencies in Ω_k. Proving the correspondence of the baseband subset from $\widehat{\Upsilon}$, with the envelopes of subset vector at the harmonic frequencies in the DTFT.

At the end, low-pass O-splines and their derivatives are encountered in the vectors of the Taylor operator $\widehat{\Upsilon}_k$ of the equation 2.21,

$$\widehat{\Upsilon}_k = \Upsilon_k (\Upsilon_k^H \Upsilon_k)^{-1} = (\Upsilon_k^{-1})^T, \tag{2.21}$$

which corresponds to the transpose of the inverse Taylor operator. So, at the end, equation 2.21 is

$$\widehat{\Upsilon}_k = \frac{adj(\Upsilon)^T}{|\Upsilon|} = \frac{Cof(\Upsilon)}{|\Upsilon|}. \tag{2.22}$$

When using Taylor-Fourier operator over the analysis equation, the reduction in computational burden is achieved. In this case, equation 2.23 is obtained,

$$\widehat{\xi} = \widehat{\Phi}^H x = \frac{\Omega^H}{N} \widehat{\Upsilon}^H x, \tag{2.23}$$

where the $\widehat{\Upsilon}^H x$ product has $K+1$ segments of N data. Every segment is formed with all Hadamard products summation of the O-splines' cyclic pieces, corresponding with the pieces of the x signal. The first product contains the pieces of the O-splines, the second their first derivative, and so on. By multiplying the former product with $\frac{\Omega^H}{N}$, the result is the Discrete Fourier Transform (DFT) divided into N cyclic pieces.

2.3.3 Impulse Response, Frequency response and Low-pass differentiators

To understand the behavior of the DTFT filters, one can observe their impulse responses, which are the modulated versions of the low-pass filters in $\widehat{\Upsilon}_k$.
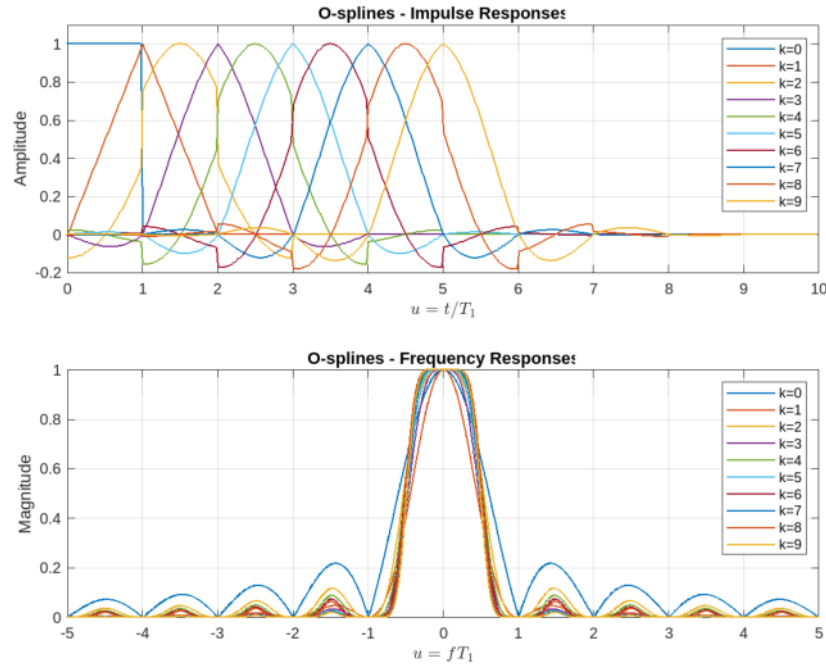
Figure 2.2: O-splines of order k = 0, . . . , 9. On the top, the impulse responses of the splines and at the bottom their frequency responses.

The $\widehat{\Upsilon}_k$ matrix is $(k+1)N \times (k+1)N$ of dimensions with diagonal submatrices. Its first vector corresponds to the impulse responses of the low-pass filter, which are the O-splines; the second vector to the first low-pass differentiator (derivative); the impulse responses from the second differentiator to the third vector and so on.

To plot the impulse responses, it is necessary to first defined the number of samples per cycle (N). In the next figures, the impulse responses of varying k-th order were plot using $N = 20$ samples per cycle. Figure 2.2 shows the impulse and frequency responses from the $k = 0$ until $k = 9$ order O-splines.

Note at the top plot of figure 2.2 the impulse responses start with the zero-th order O-spline, which corresponds to the Fourier traditional approach, and then, the impulses evolve to a cardinal sine. Consequently, in the frequency response, is interesting to see that when the order increases, the O-splines evolve into flatter pass-bands and stop-bands.
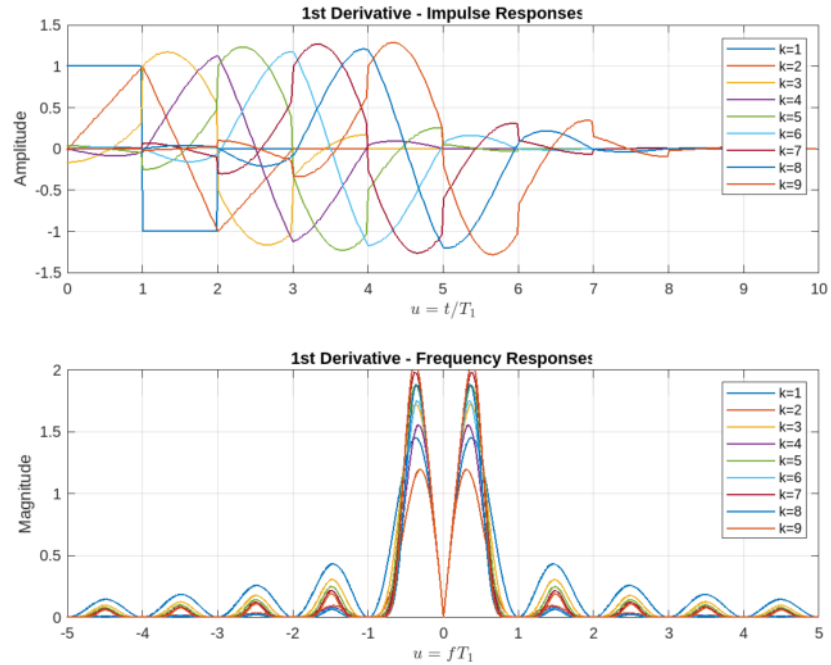
Figure 2.3: Impulse (on top) and Frequency (at the bottom) responses of first differentiators.

In addition, when designing the O-splines, it is important to consider the ideal order. As can be observed in the figure 2.2, the even-order O-splines have some discontinuities that are reflected into little sidelobes in the frequency response. On the other hand, odd orders maintain continuity and the sidelobes are normally lower.

Low-pass differentiators came from the derivatives of the previous O-spline. This operation results in more discontinuous impulse responses, as can be observed at the top of the figure 2.3, where the responses of the first differentiator are shown. In the second differentiator, the continuity is back into the model and can be observed in figure 2.4.

Both have different gain characteristics. Meanwhile, in the first differentiator the frequency response is $H_k^{(1)}(f) = (j2\pi f)^1 H_k^{(0)}(f)$, in the second is $H_k^{(2)}(f) = (j2\pi f)^2 H_k^{(0)}(f)$, representing linear and parabolic gains in their pass-bands, respectively.
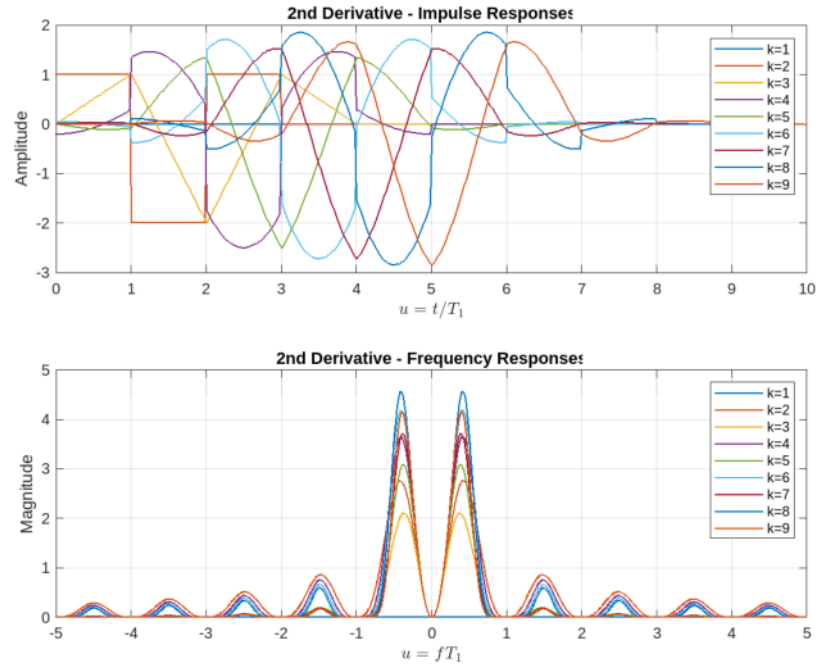
Figure 2.4: Impulse (on top) and Frequency (at the bottom) responses of the second differentiators.

2.3.4 O-splines Final Models

Finally, two O-splines' models were designed for the current work. Considering that the O-splines are Cauchy sequences that tend to a cardinal sine when the order increases, then the O-splines were selected to be of order 9 as the Euclidean distance between two O-splines and the estimated phasors is sufficiently small [63]. The normalized O-spline and its derivatives are shown in figure 2.5.

Two distinct tasks are addressed in this thesis work: the database's article [2] recreation and the state estimation analysis. The samples per cycle were set as $N = 46$ for the first task and $N = 65$ for the second. Thus, both O-splines' band-pass filters were modulated over the central frequency 11 Hz. The former covers the 8-14 Hz frequency band, and the last the band of 9-13 Hz (explanation in section 4.2.1). Equations 2.24 to 2.26
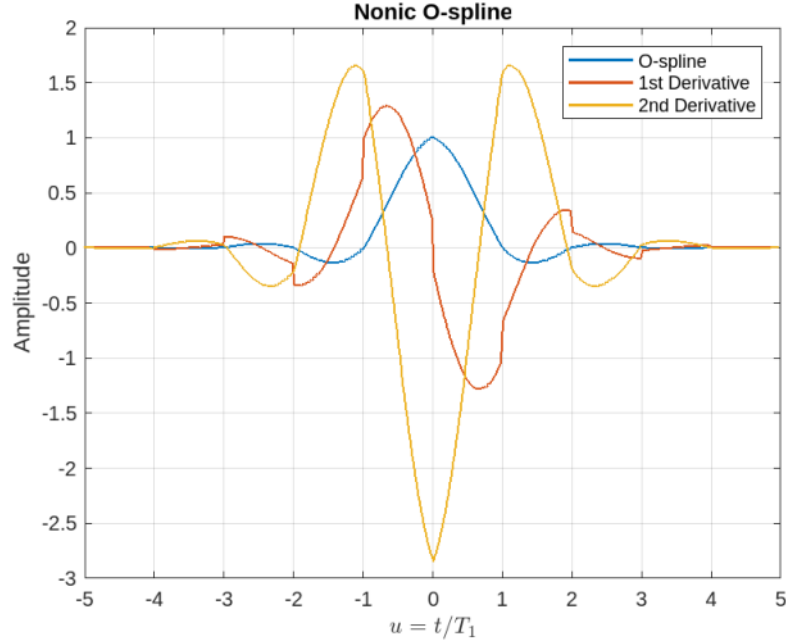
Figure 2.5: Nonic O-spline and derivatives.

were followed to obtain the frequency responses of both splines and their derivatives.

$$h = \frac{\varphi_9}{N} e^{j\frac{2\pi}{N}n} \tag{2.24}$$

$$hm = f_1 \frac{\dot{\varphi}_9}{N} e^{j\frac{2\pi}{N}n} \tag{2.25}$$

$$hmm = f_1^2 \frac{\ddot{\varphi}_9}{N} e^{j\frac{2\pi}{N}n} \tag{2.26}$$

Here, $\varphi_9, \dot{\varphi}_9$ and $\ddot{\varphi}_9$ correspond to the impulse response of the designed O-spline and its derivatives, while f_1 the fundamental frequency. In the particular case of the second O-spline, a constant factor of 1.4 was added into the exponential components of the equations for the tuning operation to the desired central frequency. Figure 2.6 shows the result of modulating both O-splines to the central frequency previously mentioned.
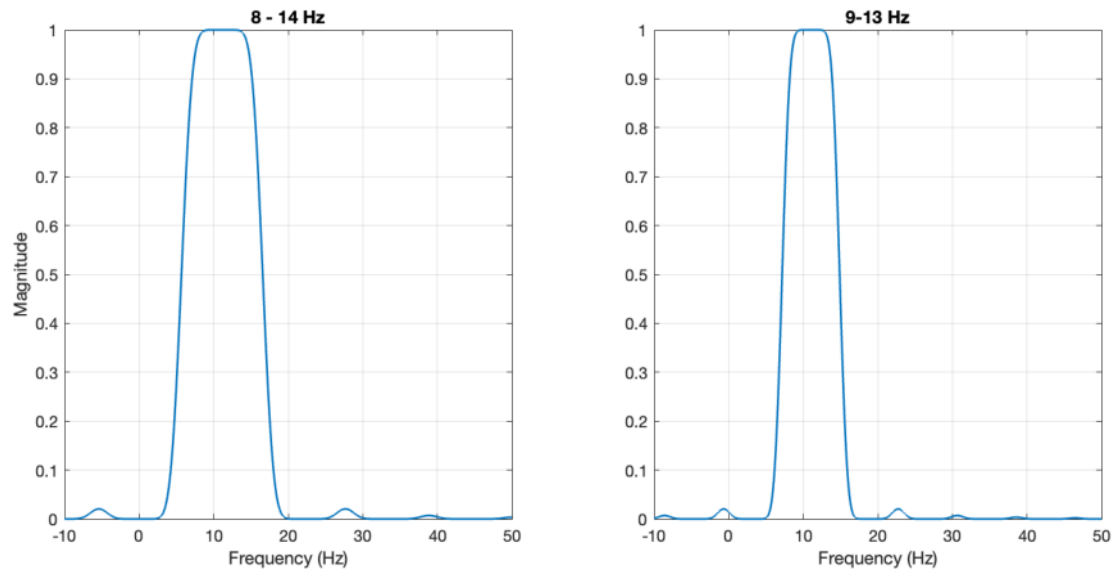
Figure 2.6: Modulated O-splines at the central frequency 11 Hz to cover 8-14 Hz band (left) and 9-13 Hz (right).

Chapter 3

Methods

3.1 Dataset

Most of MI studies have focused on classifiers performances using the well-known BCI competition datasets developed by Berlin BCI (`https://www.bbci.de/competition/`) [77, 30, 32, 36, 78]. However, even if the number of datasets is increasing, they do not normally follow the same procedure, or have the same number of classes or subject recordings. As the goal of this work is to prove the O-splines' capacity to estimate MI patterns, larger data following the same paradigm are needed.

Therefore, analysis is made using Cho and colleagues' database [2], published on `http://gigadb.org/dataset/100295`. This is composed of 52 subjects' (50 right-handed and 2 both handed) recordings performing right- and left-hand movements, as well as imaginary movement. In both cases, subjects moved and imagined moving every single finger to their thumbs. Moreover, the former-case recordings have 20 trials (in one run), while the last ones have 100 or 120 trials (five or six runs). Figure 3.1 resumes the paradigm of each trial, which lasts 7s and is divided into 3 states: pre-event for the first 2 seconds, para-event for 3 seconds, and post-event for the final 2 seconds of the trial. In the first two seconds of the observation window (-2 to 0s), a black screen
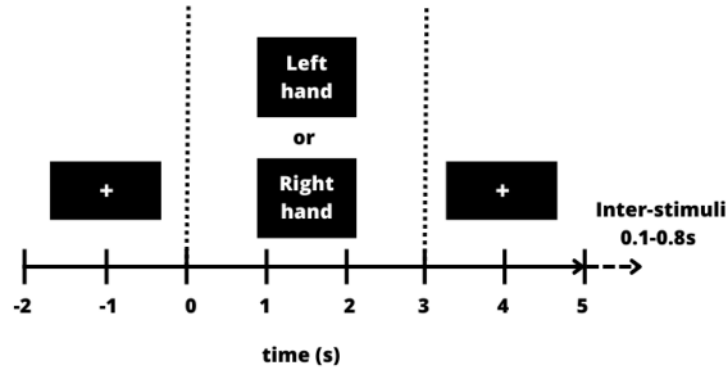
Figure 3.1: MI and movement paradigm from [2].

with a cross on the center indicated the preparation for the event. Then, the screen changed to the MI class instruction and stayed for three seconds (0-3s), being this the time of the MI-event. Finally, following the three seconds, the screen returned to the black screen for two more seconds (3 to 5s). Inter-stimuli time was set randomly between 0.1 to 0.8s.

Biosemi ActiveTwo device was utilized to obtain the brain signals with 64 AgCL active electrodes according to the 10/10 international system. Two extra electrodes were positioned over the *flexor digitorum profundos* and *extensor digitorum*, from both hands for recordings of EMG to check if actual hand movements were performed. Sample rate was set to 512 Hz for both recordings.

In addition, the database not only contains the EMG and EEG signals from all subjects, but it also keeps recordings from resting state (60 seconds) and six different artifacts such as eye blinking, eyeball movement (up, down, left, and right) and jaw clenching (twice each kind of artifact during 5 s). In all cases, the subjects were sitting in a chair in front of a screen and the room noise level was 37-39 dB. Finally, authors added a .xlsx file with answers from every participant to a self-made subjective psychological and physiological questionnaire.

The datasets contain a great amount of information to manage. For this work, all

52 subjects' recordings were considered, and only the recordings of the five/six runs of right (RH) and left hand (LH) MI were used. Recordings from channels C3 and C4 were utilized, as these two electrodes showed contralateral behavior when performing RH- and LH-MI, respectively [18].

3.2 Methodology

Signal analysis was separated into two tasks: 1) ERD/ERS quantification using amplitude modulation method [4] for recreation of [2], and 2) amplitude, phase, frequency and ROCOF estimations with O-splines. In both cases, special attention was given to the **para-event** time for characterizing the MI event apparition.

3.2.1 ERD/ERS quantification

AM has proven to be an equivalent ERD/ERS estimator with better time resolution by using only the amplitude of a complex envelope given to band-pass signals [4, 22]. In this matter, ERD/ERS quantification performed by Cho and colleagues' [2] is considered as the traditional estimation approach to compare against the O-splines technique. Therefore, the methodology presented in figure 3.2 was designed considering only the ERD/ERS quantification steps from the last-mentioned study.
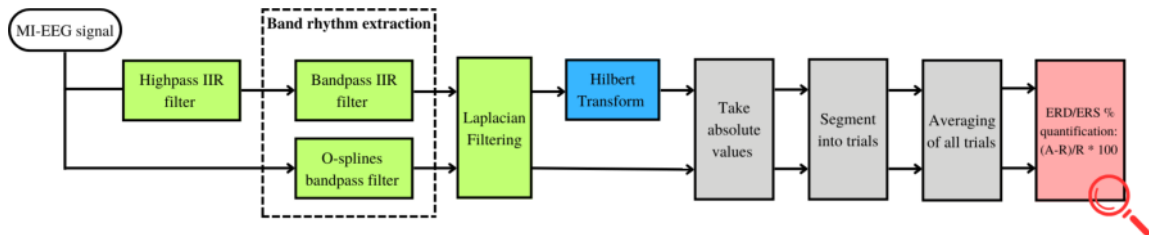
Figure 3.2: Methodology for ERD/ERS quantification using amplitude modulation and O-splines.

MI-EEG signals were filtered by two filters: 4-th order Butterworth and the O-spline.

The first one uses a high-pass filter with cut-off frequency at 0.5 Hz and a band-pass one on the 8-14 Hz frequency band. For the second method, the band-pass filter can be modulated at a central frequency of interest as described in chapter 2. Furthermore, it was centered at 11 Hz and covered the same frequency band as the Butterworth one. After this step, small Laplacian filtering [79] was performed on C3 and C4 electrodes from both filters output. Mean information using channels C1, C5, FC3 and CP3 was calculated and then, subtracted to the first electrode, while the mean from electrodes C2, C6, CP4 and FC4 was used for the second. Figure 3.3 shows the electrodes used for this operation.
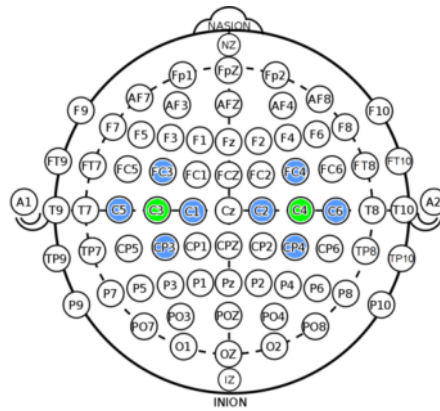
Figure 3.3: Electrodes selected for small Laplacian.

The output of the Butterworth filter passed through the HT to obtain its complex envelope. While this was not necessary in the O-splines' output signal since it is implemented as a complex FIR filter. Absolute values were taken, as only the amplitude modulation of the band-pass signals were considered in this ERD/ERS analysis approach. At the end, both signals were segmented among all of the 100/120 trials, all of these were averaged to obtain one response per subject, and the relative change baseline correction was applied to the averaged ERD/ERS pattern according to equation 3.1,

$$ERD/ERS\% = \frac{A - \overline{R}}{\overline{R}} \times 100, \tag{3.1}$$

where *A* refers to the average MI-related trials, and $\overline{R}$ is the mean value of the information in the time range of reference set between -500ms to 0ms. This correction has been proposed and used for measuring energy decreases in different MI studies [1, 3, 80, 81, 24, 82].

3.2.2 State Estimations

3.2.2.1 Spectral Region of Interest

Before starting estimation analysis, it was necessary to observe the spectral Region of Interest (ROI) corresponding to the MI activity in all recordings. Continuous Wavelet Transform (CWT) is a useful technique capable of capturing low- and high-frequency segments of the EEG signal by convolution it with adaptive windows [70]. Therefore, CWT was used to visualize the averaged ERD/ERS scalograms related to the whole database. Figure 3.4 describes the steps for this analysis.
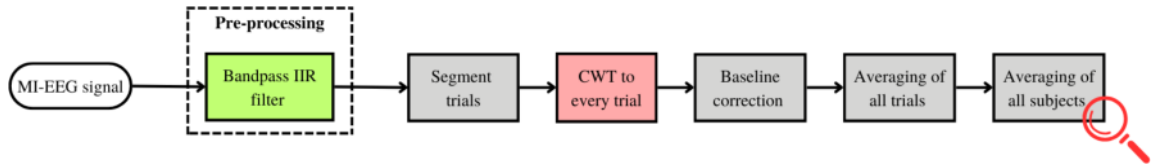
Figure 3.4: Methodology to obtain the ROI from the whole dataset.

One band-pass 4-th order Butterworth IIR filter was used with half power frequencies from 0.5 Hz to 50 Hz with the idea of observing activity from the whole spectrum of frequencies until the low gamma band (<50 Hz). Signals were then segmented into the 100/120 trials and the CWT was calculated for each of them using equation 3.2 [70],

$$X(t, \alpha) = CWT\{(x(t)\} = \int_{-\infty}^{\infty} \frac{1}{\sqrt{\alpha}} x(\tau) \psi * \left(\frac{1}{\alpha} (\tau - t) \right) d\tau, \tag{3.2}$$

where α is a scaling factor, τ controls the time domain translation of position, and $\psi \left(\frac{1}{\alpha} (\tau - t) \right)$ represents the mother wavelet, which for this analysis, Morlet wavelet from

equation 3.3 is used.

$$\psi(t) = e^{\frac{-t^2}{2}} e^{j2\pi f t} \tag{3.3}$$

Here, $e^{j2\pi f t}$ represents a sinusoid weighted by $e^{\frac{-t^2}{2}}$, a Gaussian kernel with no sharp edges.

Furthermore, baseline correction by subtracting the mean value from the time reference period of -1500 ms to 0 ms was performed to each time-frequency trial map. Finally, maps were averaged between all the 100/120 trials and then, between all 52 subjects (grand average).

3.2.2.2 State estimations with O-splines

Knowing the estimation capacity of the O-splines [60, 68], which was previously used in bio-signals [67, 83], the final task of this work looks to augment previous insights [20, 56, 81, 84] on amplitude, phase, and frequency features using this novel technique. Figure 3.5 shows the analysis made for obtaining amplitude, phase, frequency, and ROCOF estimations for each and all subjects.
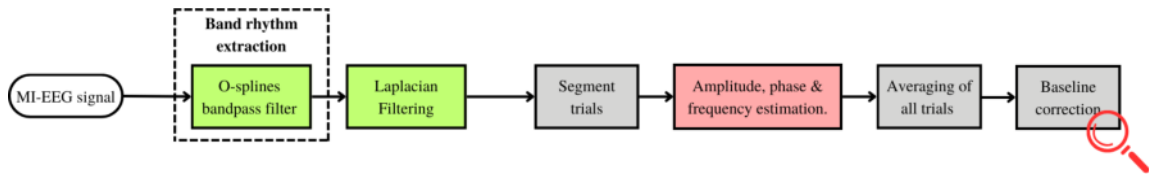
Figure 3.5: Methodology for amplitude, phase, frequency, and ROCOF estimations using O-splines.

Once the ROI was visualized after the previous analysis, the MI-EEG signals went through the O-spline filter described in the past chapter. Furthermore, small Laplacian was applied over C3 and C4 electrodes in the same way that was made for the ERD/ERS quantification task (subsection 3.2.1). Signals were segmented into trails and then, estimations were made for each trial using equations 3.4, 3.5 and 3.6. The math demon-

stration is presented in **appendix A**, and a more detailed background can be found at `https://github.com/timmyfaraday/TaylorFourierTransform.jl/blob/master/docs/src/math.md`.

$$a = 2|\xi| \qquad \varphi = \angle\xi \tag{3.4}$$

$$\dot{a} = 2Re\{\dot{\xi}e^{-j\varphi}\} \qquad \dot{\varphi} = \frac{2}{a}Im\{\dot{\xi}e^{-j\varphi}\} \tag{3.5}$$

$$\ddot{a} = 2Re\{\ddot{\xi}e^{-j\varphi}\} + a\dot{\varphi}^2 \qquad \ddot{\varphi} = \frac{2}{a}[Im\{\ddot{\xi}e^{-j\varphi}\} - \dot{a}\dot{\varphi}] \tag{3.6}$$

Here, a represents the instantaneous amplitude estimation and φ the instantaneous phase. With them, their first and second derivatives indicated by the number of dots. At the end, all estimations were further averaged to obtain one subject representation. These two final steps were done in this order as it has been stated that averaging epochs in time could result in losses of phase and frequency information relevant in MI analysis [70]. Therefore, averaging followed the estimation step and subtraction baseline correction (-1500 to 0 ms) was made at the end. The figure 3.5 shows this procedure.

3.2.3 Statistical Analysis

To give statistical relevance to the results, some hypothesis tests were performed. First, Shapiro-Wilks test was performed to observe normality in data. After it, paired t-test was used in the case of normality and Kruskal-Wallis non-parametric test for data following any other distribution but the normal one. In both cases, these were performed for finding significant differences between electrodes or methods.

In the cases of ERD/ERS patterns and state estimations, a mean value calculated from the samples of **para-event** time (0-3000 ms) was extracted and used in the tests. For filters comparison, a distortion rate was calculated from the PSD of each averaged ERD/ERS pattern.

3.2.4   Classification

Lastly, a classification step was done to compare the performance of the two methods and when using the O-splines' extracted features. In this matter, three different linear classifiers were used: linear Support Vector Machine (L-SVM), Logistic Regression (LR) and Linear-Discriminant Analysis (LDA).

In the same way that statistical analysis, the mean value from the samples of the para-event time was obtained for every subject. However, input arrangements were different according to the task. On one hand, the input array using ERD/ERS patterns data considered both C3 and C4 electrodes and had 104 samples (52 observations x 2 electrodes) for each MI-class (RH and LH). On the other hand, the one from the state estimations was composed of only the information from electrode C3 and had 312 samples (52 observations x 6 features) for each MI-class.

On both cases, 5-fold cross-validation was used to train the models, and 25% of the observations (13 observations) from the 52 related to each participant were separated for testing the models. At the end, classification accuracy (ACC) was the parameter obtained for measuring performance.

Chapter 4

Results

For results, signal analysis was undertaken under MATLAB environment, in particular EEGLAB [85] toolbox. This toolbox refers to an open-source software for electrophysiological signal analysis and was used for trials segmentation and topography plots. Signal processing and statistical toolboxes were also used for filter design and statistical analysis, respectively. Classification Learner app in MATLAB was utilized for classification models training and testing. O-splines were programmed in MATLAB in accordance with equations and code lines presented in [63]. Finally, only Shapiro-Wilks normality tests were programmed in Python language using *SciPy* library.

4.1   ERD/ERS analysis

This first analysis examined the variations in amplitude of the MI-EEG signal delivered by the complex envelope of an analytic signal. Both methods filtered out the original signal to extract only the information from the alpha and lower-beta bands (8-14 Hz). The HT was used to generate the analytic signal on the Butterworth-filtered signal, while the O-spline-filtered analytic equation was obtained with the convolution operation. After segmentation of trials, averaging of all 100/120 trials and baseline correction,

ERD/ERS patterns were obtained. The figure 4.1 shows the ERD/ERS quantification map for RH- and LH- MI, using both Butterworth and HT (Bw+HT) and the O-splines.
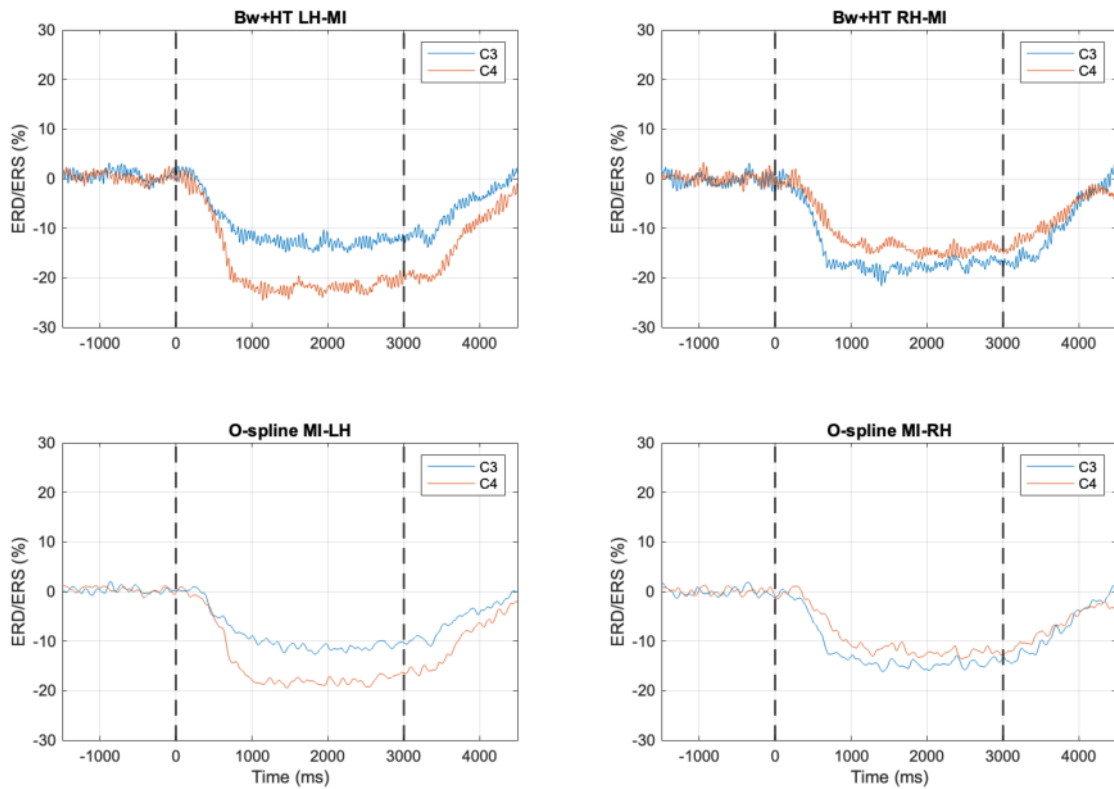
Figure 4.1: Grand average ERD/ERS estimations using traditional method (upper row) and the O-splines (lower row). LH-MI on the left column, and RH-MI on the right one.

The main difference between both techniques is the clarity of the ERD pattern captured in **para-event** state. The traditional approach maintained high frequency oscillations during the whole observation window (-1500-4500ms), while with the O-splines, the ERD event is clearer. Although, both methods could capture the ERD pattern inside the para-event time (0-3000 ms) around the 200 ms, as well as the ERS one after the 3000 ms event.

Moreover, the ERD pattern from the O-splines indicated decreases in both C3 and C4 electrodes for both RH- and LH- MI. A greater decrease in the amplitude is observed

on C4 (red) than on C3 (blue) while performing LH-MI, and vice-versa when performing RH-MI, confirming the contralateral behavior seen in MI studies. Nevertheless, both C3 and C4 electrodes had similar and closer amplitude decrements while performing RH-MI in all cases presented in the figure, while channel C4 estimation had 10 % larger desynchronization when LH-MI was performed.

Regarding the activation zones during the MI-event, the figure 4.2 shows a series of topography plots with the mean value of the para-event time samples from both methods. From the figure, it can be observed that the ERD was present majorly over the sensorimotor central cortex due to the MI-event being processed, as well as on the occipital cortex because of the MI-paradigm, in which participants were observing a monitor waiting for the signal cue.
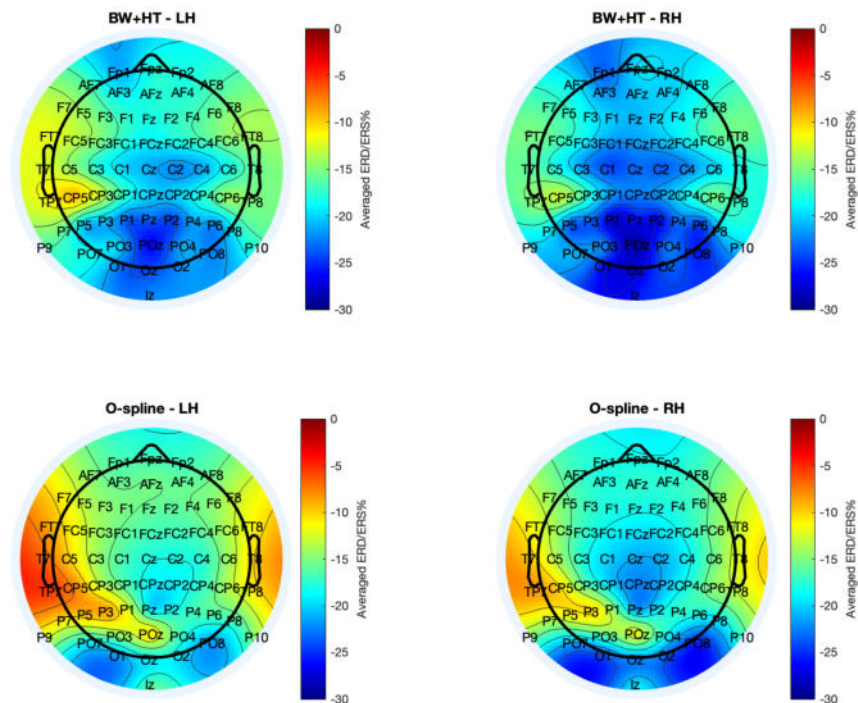
Figure 4.2: Topography plots of the grand average ERD. On the top row, the distributions from the Bw+HT data. At the bottom row, distributions of data from O-splines. For this representation, Laplacian spatial filter was not performed. The rest of step had the same configurations.

Nevertheless, some differences between methods are evident. Firstly, the ERD quantified by the Bw+HT method (upper row) seems to be more disperse over the whole central area from the occipital (channels Ox) to the prefrontal cortex (channels Fpx) during RH-MI. However, when performing LH-MI, the areas where the ERD is present were reduced, and the major activation activity appeared over central (Cx and CPx), parietal (channels Px), and occipital areas.

Turning now to the data from O-splines (lower row). The figure shows a more concentrated distribution over both occipital and sensorimotor areas. On LH-MI, participants had difficulties to induce the ERD, and only around -20% of desynchronization is illustrated over central zones (Pz, CPz and Cz) and contralaterally on (P2, CP2, C2). During RH-MI, larger percentages of desynchronization (> -20%) were found on the central area (Pz, CPz, CP1, CP2 Cz, C2, C1, C3, C4, FCz) instead of contralaterally.

A comparison between these two methods reveals that the O-splines separated the activation zones in a better way than the traditional method, where ERD seemed to be present over the whole central cortex.

With these results, Shapiro-Wilks test looked for normality in data. Table 4.1 shows the p-values for both methods. In all cases, the ERD quantification values followed a non-normal distribution. Therefore, Kruskal-Wallis was used for significant differences between methods in all electrodes and MI classes. Test delivered **non-significant differences** among the estimation **($p > 0.05$)**.

Table 4.1: p-values from Shapiro-Wilks test of normality using mean values from para-event MI state.

	p-values			
Method	**RH**		**LH**	
	C3	**C4**	**C3**	**C4**
Bw+HT	0.000655	0.009459	0.000187	0.012329
O-splines	0.000297	0.002536	0.000286	0.000389

4.1.1 Filters comparison

To evaluate the filters effect to the signal, a distortion rate (DR) feature was evaluated using the power spectrum density (PSD) of each of the subject's averaged ERD/ERS pattern. This is described in equation 4.1 and refers to the rate of the amount of energy from other frequencies (or non-desired energies, E_{nd}) inside the frequency band of interest (or desired energy, E_d). On one hand, a value close to 0 means that the band of interest has no affectation from other non-desired frequencies. On the other hand, if the value increases, it refers to the presence of the energy from other bands inside the one of interest.

In this measurement, the desired energy corresponded to the 8-14 Hz band, and the non-desired energy frequencies were all those above 14 Hz.

$$x_{DR} = \frac{E_{nd}}{E_d} = \frac{\sum_{n=1}^{N} x_n^2}{\sum_{m=1}^{M} x_m^2} \tag{4.1}$$

In equation 4.1, x_n refers to the coefficients from all non-desired frequencies and x_m to the desired frequency band from the vector obtained using 2^{12}-points FFT.

Figure 4.3 shows the boxplot distribution of the 52 subjects' DR values for C3 and C4 electrodes on both MI tasks. Filters capacity differences became apparent when observing these values, as the signal from the **O-splines** had values **closer to 0 and around 0.7**, while the signal from **Butterworth had bigger rates** (> 3). This indicates the presence of higher frequencies inside the band of interest while using the last filter.

To explain this phenomenon, the PSD of the subject 14's averaged ERD/ERS pattern from electrode C3 is shown in figure 4.4. It is noted that the O-splines filtering capacity had greater effect as only low frequencies and the frequency band of interest had higher peaks (this due the averaging operation of all trials). Contrary to this, the PSD of the signal from Butterworth showed larger harmonic presence of higher frequencies inside the signal.
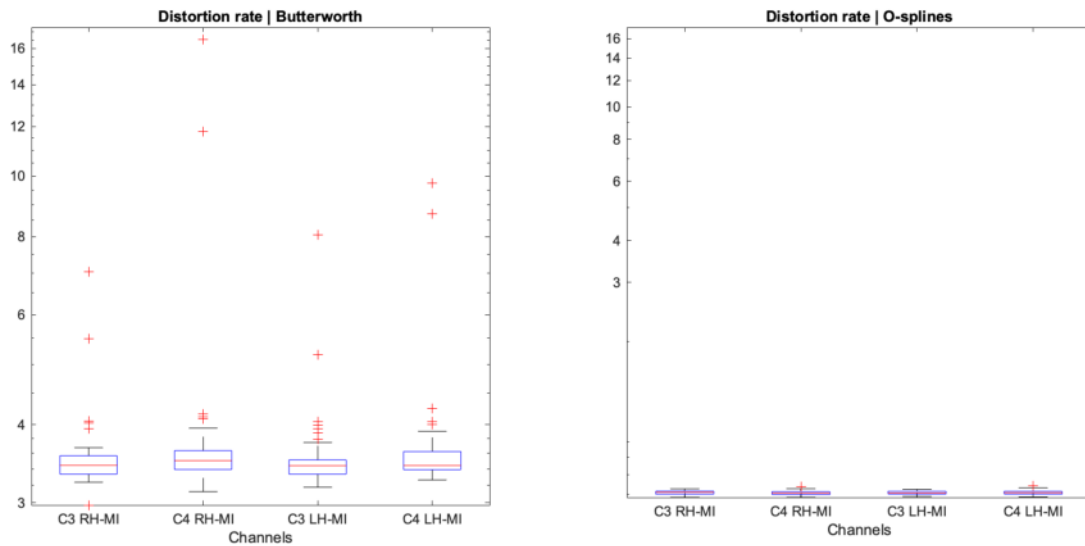
Figure 4.3: DR distribution of the 52 subjects' on C3 and C4 electrodes while performing RH- and LH-MI.
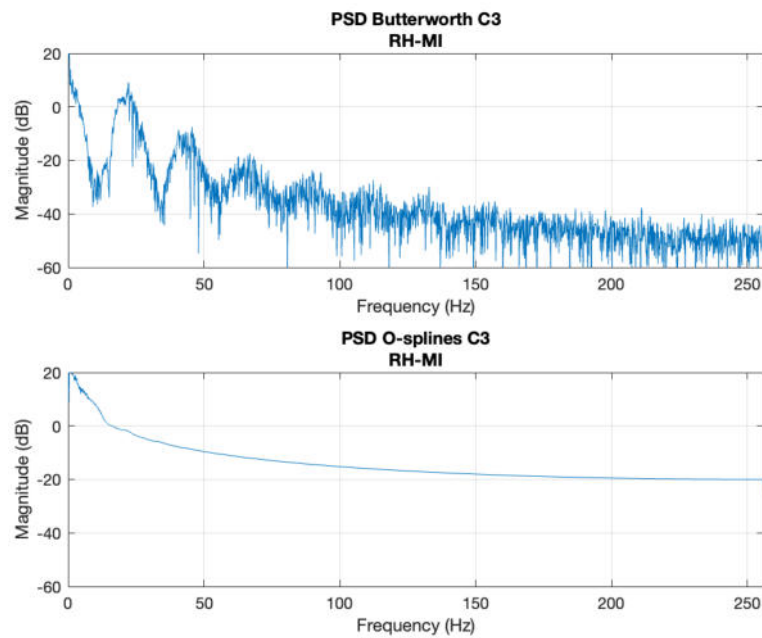
Figure 4.4: PSD of the C3 electrode mean ERD/ERS pattern while performing RH-MI from subject 14 using Butterworth (up) and O-spline (down).

Table 4.2: *p*-values after Shapiro-Wilks normality test using DR values.

Filter	RH		LH	
	C3	**C4**	**C3**	**C4**
Butterworth	0.000000	0.000000	0.000000	0.000000
O-splines	0.496566	0.723566	0.202217	0.141203

Table 4.3: *p*-values after Kruskal-Wallis and paired t-test tests over C3 and C4 channels for each method.

p-values		
Filter	**RH**	**LH**
Butterworth	0.049605	0.145319
O-splines	0.397168	0.599603

Statistical analysis showed a normal distribution when using data from the O-splines ($p > 0.05$), and non-normal distributed data from Butterworth ($p < 0.05$). Table 4.2 has the *p*-values for each electrode while doing both MI tasks. Moreover, significant differences between electrodes C3 and C4 and between methods were also looked. Kruskal-Wallis was performed for differences between electrodes from the Butterworth filter and paired t-test from the O-splines ones. Table 4.3 shows the *p*-values. DR values from the O-splines channels had non-significant differences ($p > 0.05$), while those from Butterworth showed significant differences during RH-MI ($p < 0.05$) and non-significant differences on LH-MI ($p > 0.05$). When **comparing both filters**, paired t-test showed **significant differences ($p < 0.05$)** in all cases.

4.2   State Estimations

4.2.1   Region of Interest (ROI)

The ROI analysis considered only C3 and C4 electrodes for both motor imagination of RH and LH. Note in figure 4.5 that the energy is present mostly around the 8-14 Hz

frequency band (11 Hz particularly) and that, after the cue at 0 ms, it decreases in all four cases. Low energy is maintained until the MI-trial is finished after 3000 ms, when it increases.
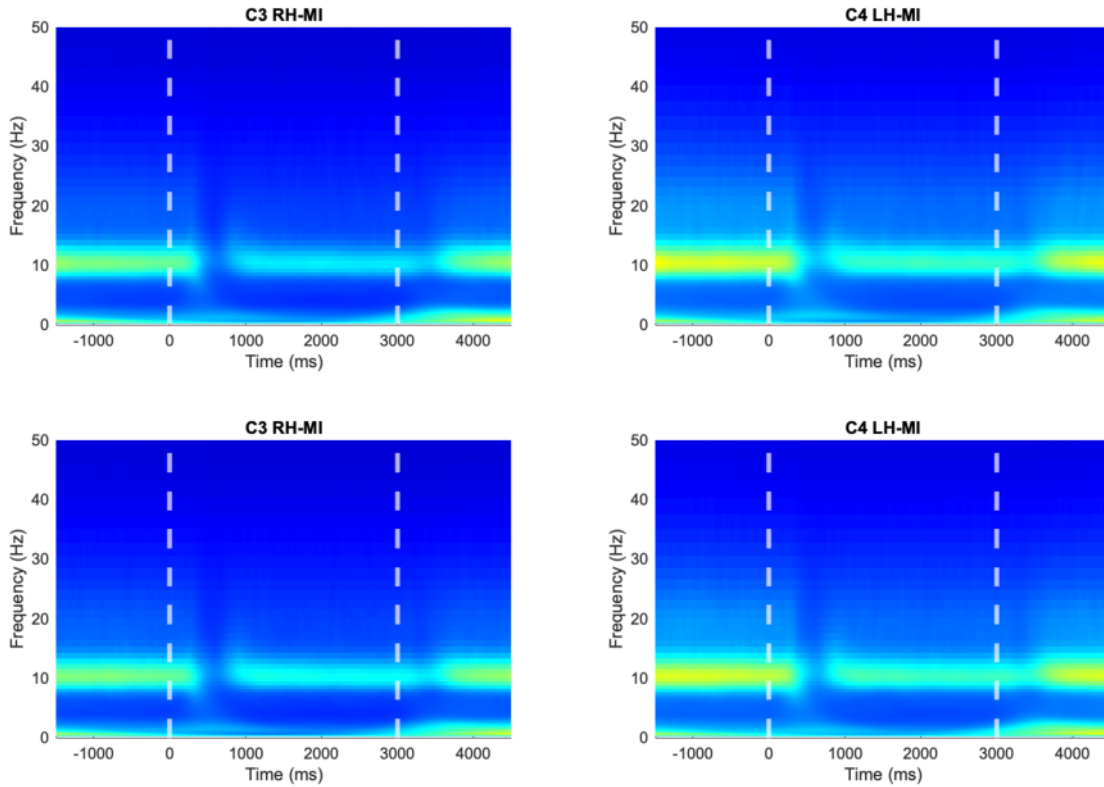
Figure 4.5: Grand average energy maps of MI-events.

After baseline correction, the desynchronization events seen in figure 4.6 occurred on the 9-13 Hz frequency band and lasts around the same time that the energy increases presented in figure 4.5. This indicates major presence of MI activity inside this band. Therefore, the O-spline design (described in section 2.3.4) and the state analysis were made using these specifications.
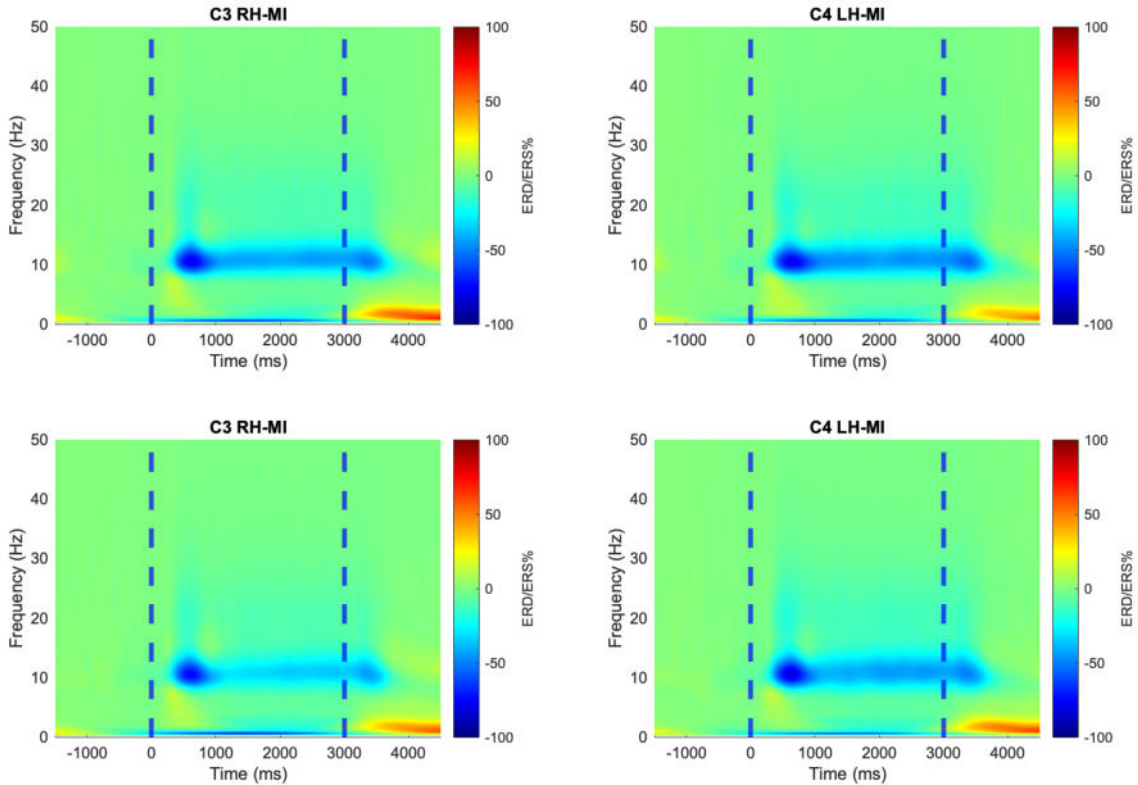
Figure 4.6: ERD/ERS maps using subtraction baseline correction.

4.2.2 Amplitude, phase, frequency and ROCOF estimations

State estimations of MI-events with O-splines become another contribution from this work to the field. Figure 4.7 shows the grand average ($n = 52$) state estimates of the RH-MI events after subtraction baseline correction. On the left column of the figure, the amplitude estimation delivered a similar behavior to the first ERD/ERS quantification map in figure 4.1, having decreases and increases in amplitude around the same marks of time: 700 ms and 3500 ms. First and second derivative of amplitude added oscillation and energy information, respectively.

Similarly, grand average phase estimation and its derivatives such as Frequency and ROCOF on the right column of the figure were captured. Firstly, C3 and C4 electrodes had their magnitude differences, as it was captured that the phase from C3 had larger
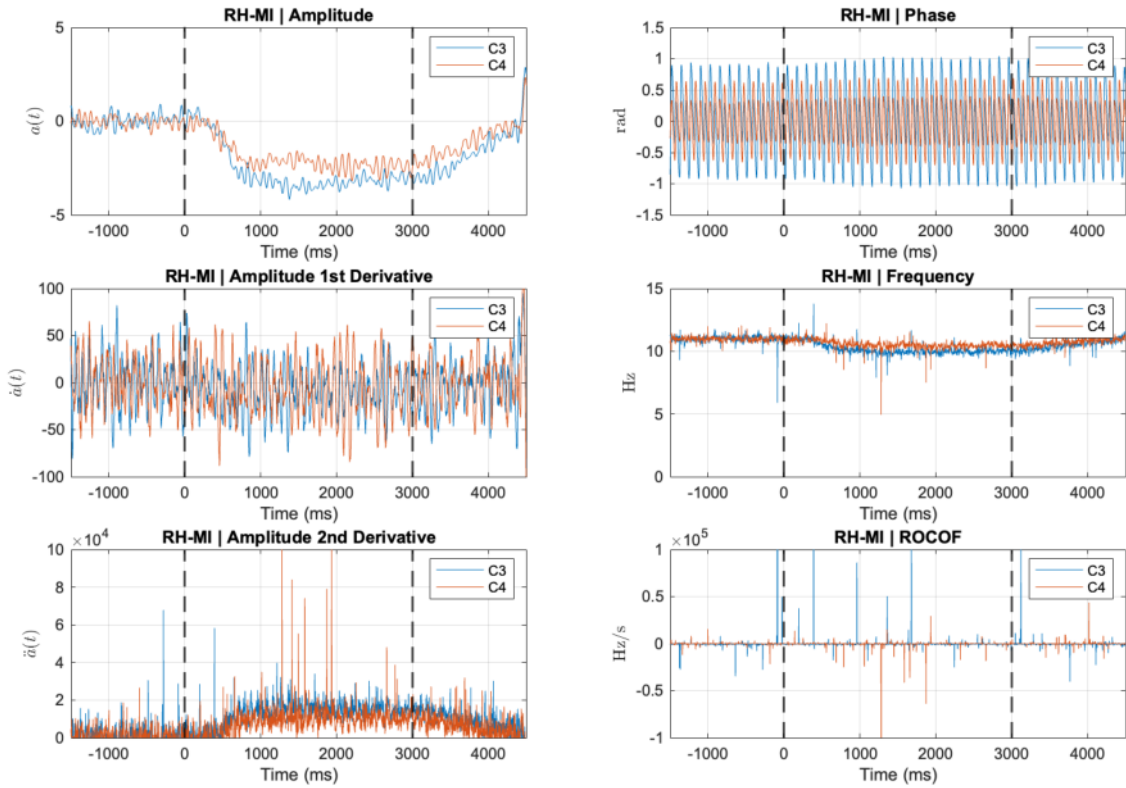
Figure 4.7: Grand average state estimations of RH-MI.

displacement than the one from C4 in the whole observation window. Although C3 phase estimation movement was shortly larger at the MI event than its pre-event state. For frequency, results showed estimations around 10 Hz on electrode C3 at the moment of the event. C4 frequency estimation followed the behavior in a lower way. Finally, ROCOF quantified several peaks mostly present at the time of the MI-event, indicating larger changes in frequency during this time. Particularly, one positive peak around the 500 ms event on C3 represents the change in frequency visualized in the frequency plot, as well as the negative peak seen close to the 4000 ms event.

Now, looking into the LH-MI state estimates, the Figure 4.8 shows the results. Starting with amplitude on the left, all estimations seem to be equal to those in figure 4.7, yet they are not. In this case, C4 amplitude envelope had larger decrease than C3, which
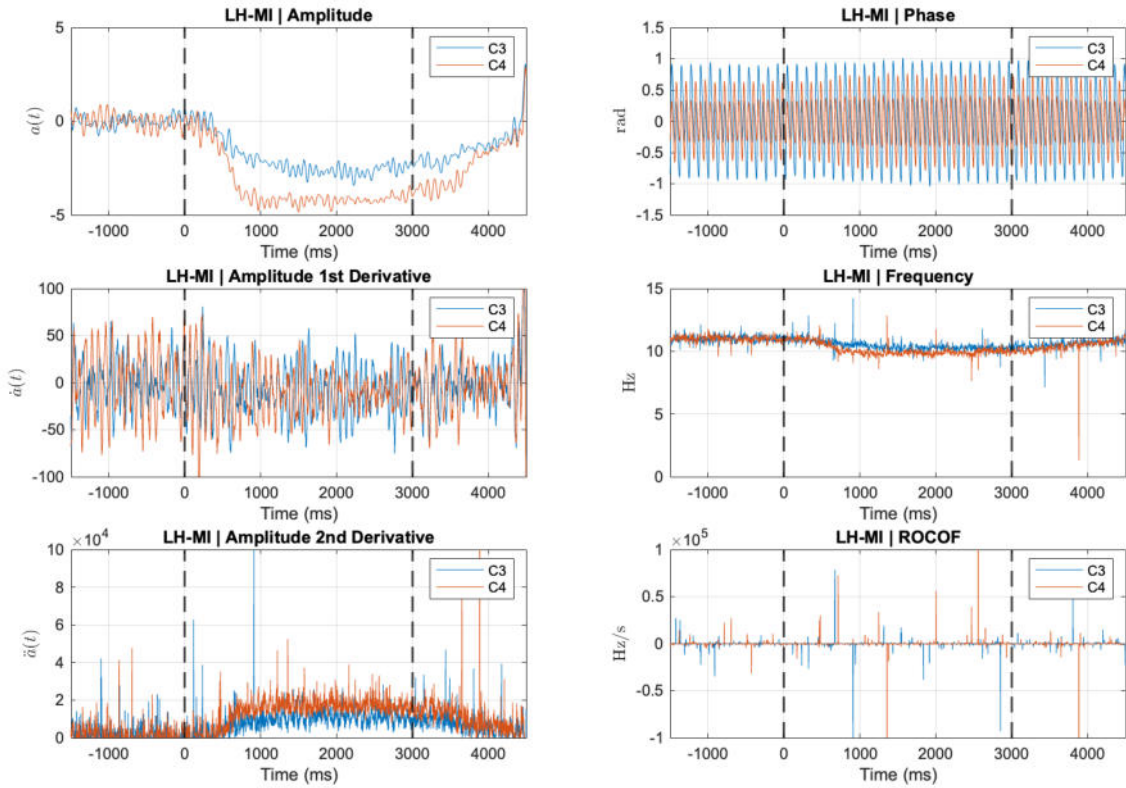
Figure 4.8: Grand average state estimations of LH-MI.

confirmed the contralateral behavior expected from these signals. Oscillations in the first and second derivatives also maintained this behavior at events collected from electrrode C4.

On the other hand, phase variations show larger movements at the MI-event time for both electrodes in comparison with the time of reference. Frequency estimation showed activity over 10 Hz on C4 channel events, while C3 ones remained close to these, which was similar to the RH estimation in figure 4.7 but keeping the lateralization behavior. ROCOF delivered the presence of two major positive peaks in both electrodes around 700 ms, corresponding to the change of frequency between 10 Hz and 11 Hz. Besides, a larger negative peak in C4 was encountered close to the 4000 ms event. And finally, during the MI trial, several peaks were also found with no greater changes in

Table 4.4: *p*-values after Shapiro-Wilks normality test for both MI tasks and electrodes using information of MI event time.

p-values				
Feature	**RH**		**LH**	
	C3	**C4**	**C3**	**C4**
Amplitude	0.000000	0.040197	0.041557	0.000001
Amplitude 1st D	0.024007	0.813016	0.587947	0.015163
Amplitude 2nd D	0.197160	0.129141	0.124345	0.027546
Phase	0.000000	0.000000	0.000000	0.655283
Frequency	0.000000	0.000000	0.012445	0.004962
ROCOF	0.000000	0.000000	0.000000	0.000000

Table 4.5: *p*-values after one-way Kruskal-Wallis test of all six estimations from O-splines.

p-values		
Feature	**RH**	**LH**
Amplitude	0.860662	0.835200
Amplitude 1st D	0.764898	0.804873
Amplitude 2nd D	0.830126	0.942989
Phase	0.886270	0.799846
Frequency	0.820003	0.701297
ROCOF	0.922316	0.937817

frequency.

Normality test using Shapiro-Wilks indicated non-normality in almost all cases from all six different features delivered by the O-splines. Table 4.4 shows the *p*-values for each characteristic at both MI classes. Kruskal-Wallis test for differences between electrodes showed non-significant differences between the estimations on each of the features. Table 4.5 resumes this.

4.3 Classification

Finally, in an extra step for measuring the results, data from both methods' ERD/ERS patterns and the six different features from the state estimations task were extracted

and introduced into three linear classification models. The tables 4.6 and 4.7 present the summary of classification results on both tasks of the work.

Table 4.6: Classification results using data from the ERD/ERS analysis. 5-fold cross-validation was used for validation results, and 25% percent of observations (13 observations) were used for testing.

	Classification Accuracy (%)			
	ERD/ERS			
Models	Bw+HT		O-splines	
	Validation	Testing	Validation	Testing
L-SVM	62.82	65.38	62.82	**69.23**
LR	65.38	65.38	64.10	65.38
LDA	65.38	61.54	62.82	65.38

Table 4.7: Classification results using data from the State Estimation task. 5-fold cross-validation for validation results, and 13 observations were used for testing.

	Classification Accuracy (%)	
Models	State Estimations	
	Validation	Testing
L-SVM	82.05	84.62
LR	91.03	**92.31**
LDA	70.51	61.54

What stands out in table 4.6 is that using the O-splines for extracting the ERD/ERS pattern did not seem to have greater differences against results from the traditional Bw+HT. This could be expected as the models share the same data feature (the mean of the MI-event samples) that was introduced in the statistical analysis, where non-significant results were found. Although, it is of acknowledgement the increase of percentage from 65.38% to 69.23% using SVM, and 61.54% to 65.38% using LDA. The confusion matrices from both L-SVM models are illustrated on the figure 4.9, where is evident that the model had more difficulties for identifying values of LH- than RH- MI on both the validation and testing processes.

The most striking result comes from the classification accuracies in table 4.7, as
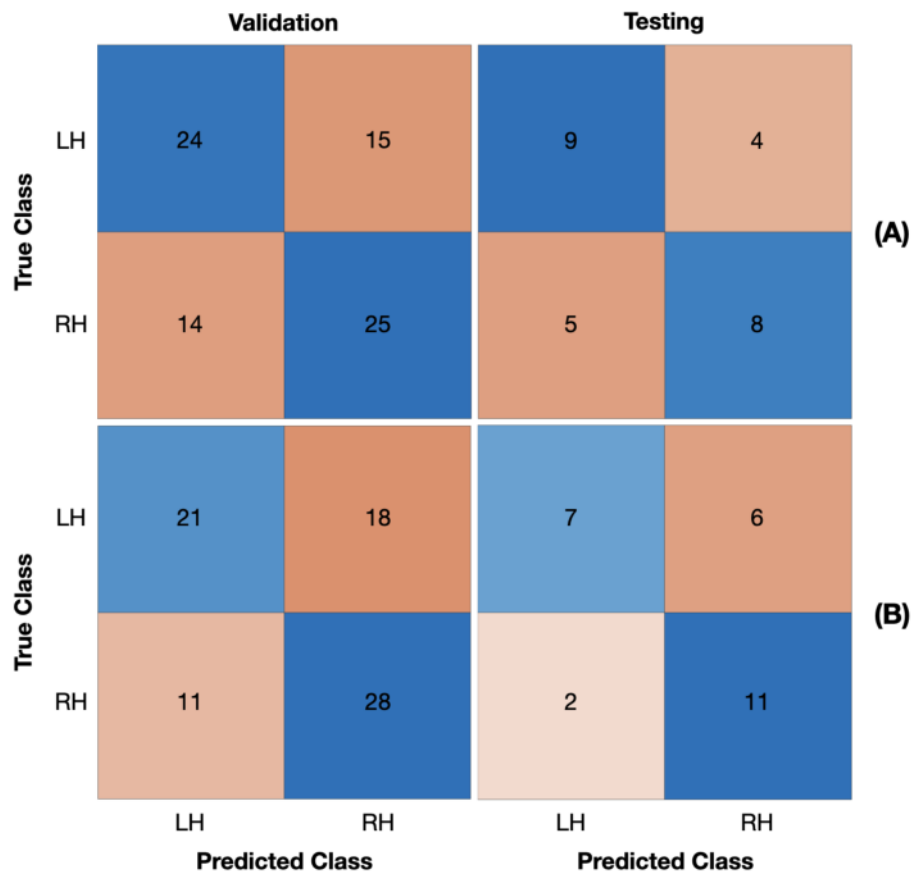
Figure 4.9: Confusion matrices for validation and testing step from L-SVM models. Row (A) refers to the confusion matrices from Bw+HT data, and (B) from O-splines data.
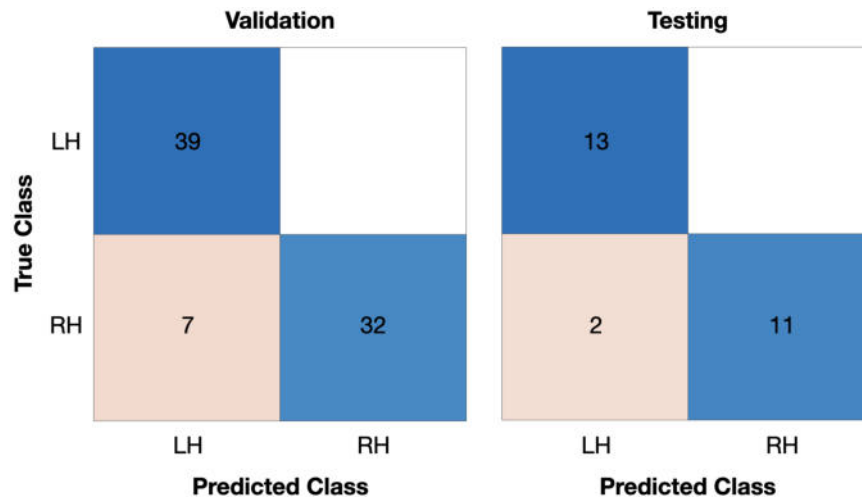
Figure 4.10: Confusion matrices from validation and test processes using LR model on state estimations data.

using the O-splines' features from the state estimation task increased the testing values largely. In this case, the L-SVM testing result delivered 84.62%, **LR** had the best result between the models with **92.31%**, and LDA had the poorer performance with 61.54%. In figure 4.10, the confusion matrices from both validation and testing steps of the LR model are presented. In here, it is surprising to see how the model could identify all values from LH-MI in both validation and testing steps, while had a few misses when classifying values from RH-MI.

In this matter, it can be observed that even if the ERD/ERS pattern obtained with the O-splines did not differ greatly from the ones by the Bw+HT method, using its features did. This is a remarkable result due that could indicate that MI-events information can be extracted with these physical parameters for obtaining more insights about this cognitive process.

Chapter 5

Discussion

The main objective of this work was set to characterize the responses and patterns obtained from using the novel O-splines method in MI-EEG signals. This was done by looking into four results: the traditional ERD/ERS pattern quantification, the effect of the filter over the signal, the state estimations using the O-splines, and classification performance between two classes of MI.

5.1   ERD/ERS analysis

With respect to the first goal, the current investigation found that the ERD/ERS patterns coming from the O-splines were clearer in comparison to the ones from the traditional method. Visually, the patterns contained less higher frequency oscillations, which indicates less affectation from other frequencies and a more approximate estimation. Normally, it is recommended to perform a soften operation for reduction of variations on the ERD/ERS pattern [3]. For example, Alzahrani and Alsaleh [86] investigated the influence of soften techniques, finding the best performance in their proposed "regularization" method. In this matter, considering that one of the BCIs' aims is to actuate with the greatest accuracy in low execution times, to add a soften operation could ex-

tend this time and much of the information could be lost. The O-splines avoided the addition of this extra step, maintaining a very approximate estimation of the patterns.

A note of caution is due here since statistical analysis showed non-significant differences in estimations between both methods. A possible explanation for this might be that, although patterns were visually different, both followed the same behavior. In other words, the general amplitude variations were captured at the same time marks where the ERD (200 ms) and the ERS (3500 ms) appeared by both methods.

One interesting finding was that with the O-splines, the grand-averaged ERD/ERS patterns were visually similar to the two resulted in the database's validation article [2]. The database **validation process** involved pre-processing steps and discarding bad trials and subjects until only 36 significant subjects remained. Using the **O-splines'** filtering and estimation capacities **allowed the inclusion of data that were discriminated before**. This permitted to use all 52 subjects instead of pre-evaluate the datasets and eliminate important data from different subjects.

Another important finding from this activity is the previously reported **contralateral behavior** in MI-EEG. In the four cases presented in figure 4.1, the electrode contralateral to the MI tasks had larger decreases in amplitude than the ipsilateral one. On one hand, during LH-MI, there was a 10 % difference between electrodes. On the other hand, when performing RH-MI, differences between both electrodes seemed minor. These results would infer that subjects were able to induce the MI event and to separate the induced activity from both electrodes zones majorly while performing LH-MI. However, this was not greatly accomplished during RH-MI, as amplitude decreases seemed to have similar percentages. This is something that could be observed on the topography plots in figure 4.2, where ERD was present over a large part of the central area during RH-MI, and on concentrated areas on LH-MI. This could be explained by the type of MI task, as subjects from the datasets performed motor imagination of fingers, and this has been described to have a bilateral effect on the mu-band (8-14 Hz)

[87].

5.1.1 Comparison of filters

The second objective of this study sought to determine if the O-splines' FIR filter could extract only the sensorimotor rhythm related to MI. This by extracting information from alpha and lower-beta bands. Previous studies evaluating the O-splines' FIR filter capacity observed consistent results on separating frequency bands information [68, 62, 64]. The findings in these studies provided further support for the hypothesis that the O-splines could performed better than other filters.

The pre-processing step is important in any BCI approach. Therefore, the correct design of filters required special attention before applying them into MI-EEG signals. One main reason that the Bw+HT approach resulted in an **oscillating signal** could be the low order of the high-pass and band-pass filters. In the work of [22], authors used the amplitude modulation approach with a **10-th order Butterworth filter**. In consequence, ERD/ERS patterns were clearer and classification accuracies were **higher than 80 %** using two different datasets. This was the principal line to use the O-splines filtering capacity in this analysis.

In this work, filters effect on the signal was measured with a distortion rate considering energy from desired and non-desired frequency bands. Results showed **rates closer to 0** from estimations coming from the **O-splines**. Otherwise, **values of distortion were larger** considering patterns from **Butterworth filter**. These values imply **significant differences** when observing spectral information instead of temporal. This was later confirmed statistically when comparing both filters **($p < 0.05$)**.

In general, averaging all 100 (or 120) trials in time caused the propagation of the spectral energies around the ERD/ERS patterns from different frequencies. The O-splines had the capacity to cut off other non-desired frequencies, while Butterworth at-
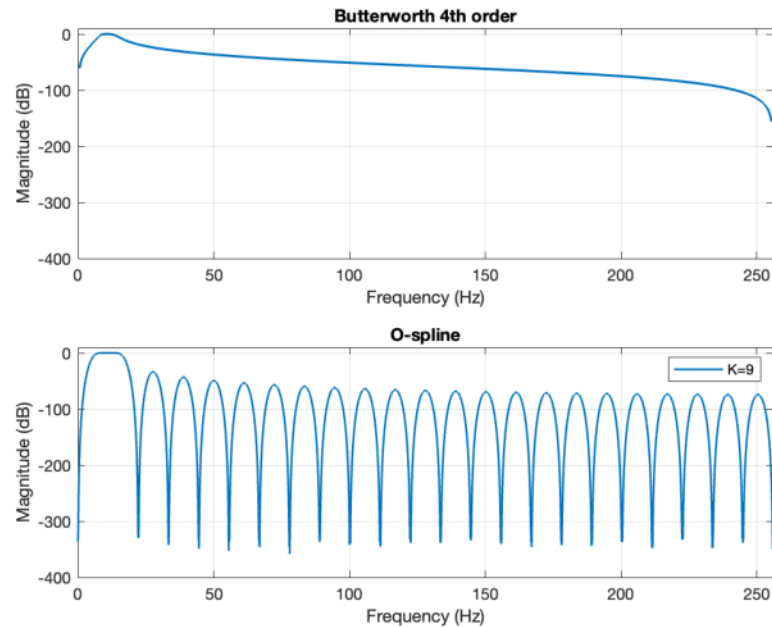
Figure 5.1: Frequency responses from each filter. While Butterworth attenuates higher frequencies around -50 to -100 dB, O-spline does it around -350 dB at the stop-band.

tenuated them in a lower manner. In consequence, when averaging all trials, the lower energies from non-desired frequencies affected more in the ERD/ERS pattern after Butterworth than after the O-splines.

The significant differences between methods could be attributed to the characteristics of both filters. In [68], the **O-splines** were designed of order 9, same as the one in this work. The study remarks the high attenuation gain values of the filter: **-34 dB** at the first **sidelobe** and **-350 dB** at the **stop-band**. In contrast, the IIR 4-th order Butterworth filter used for comparison maintained a **negative logarithmic behavior** with attenuation gains from **-10dB (close 15 Hz) to -50dB (close to 100 Hz)** on the stop-band. In figure 5.1, the frequency responses from both filters can be observed.

In addition, differences were found not only numerically speaking, but also in the methodology. Using the O-splines FIR filter saved one pre-processing step, as only

band-pass filtering was performed before Laplacian. And in the same way, no other operation (as the HT after Butterworth) was performed after. The DTFT-FIR filter approximation obtained the analytic signal from the EEG signal input, while the ideal HT was implemented through the FFT (which is its discrete time form); therefore, several steps were accomplished at the same time. This could represent computational savings into the signal processing step in BCIs, something to be reported in [83].

5.2 State Estimations

This last task was set out with the aim of assessing the state estimations capacity of the O-splines on MI events. In this matter, a few differences had to be considered with respect to the ERD/ERS quantification task: (1) the O-spline design and (2) the nature of the parameters to be extracted. Both points are discussed next.

5.2.1 Region of Interest

First, the frequency band of interest had to be chosen depending on the MI activity energy (de-)synchronization induced by the subjects, instead of setting it according to literature. Some studies have worked with the idea that the MI activity varies the frequency band where it appears according to the subjects [50, 27, 41]. Therefore, a grand-average ERD/ERS time-frequency map was obtained to work with a frequency band related to MI for all datasets.

The most obvious finding to emerge from the analysis is that the desynchronization events were found majorly inside the 9-13 Hz frequency band. This combines both alpha and beta bands, although, most of the energy activity concentrate on the alpha band. Even if the literature shows energy synchronization over beta [18], in both MI cases and for both electrodes, this was not present. Thus, the task was performed, and the O-spline design was implemented over this band.

5.2.2   Amplitude, phase, frequency and ROCOF estimations

The second point corresponds to the characteristics of the parameters obtained with the O-splines. State estimations provide spectral information as well as temporal-amplitude one. Hence, it was important not to lose this information in the averaging trials operation. Having this in mind, estimations for the time-frequency ERD/ERS maps and for states ones were made before obtaining an average representation of each subject and then, a grand-average one for all datasets.

Essentially, the amplitude estimations showed changes in both channels at the moment when the MI exercise is being performed. Two interesting findings were that the decreases obtained in the first amplitude estimation looked very similar to those in the ERD/ERS quantification activity and that the second derivative of amplitude also estimated changes after the cue of the MI-event. Perhaps an unexpected result was the oscillated first derivative of the amplitude estimation, were both channels C3 and C4 had similar noise-alike behavior.

By looking into the spectral estimates, phase parameter seemed to have non-greater than one displacement. Although, little changes become apparent visually after the start and the end of the MI-event cues at seconds zero and three. Frequency estimation had a decrease from the central frequency (11 Hz) to 10 Hz. A possible explanation to this is that the observation is over the central frequency, and changes are not expected to be large. Finally, ROCOF is a very important parameter in power systems, as is used to assess synchrophasor measurements [63]. In this analysis, ROCOF marked the presence of large peaks related to the changes of frequency during the MI-event time (0-3000 ms), indicating the exact moments when the changes happened.

5.3 Classification Results

Normally, works tend to add a classification step after the signal processing process to measure the performance of their proposed methods in terms of classification accuracy. Adding this last step to the work helps visualize if the features extracted are enough for having a classification accuracy worth testing over online BCIs. Therefore, these results were also considered to give a better perspective of the range of the O-splines by using information from each of the features extracted (ERD/ERS pattern, amplitude, phase, etc.).

Contrary to expectations, the first result showed regular classification accuracy of **69.23 %** (using SVM) against the 65.38 % from the traditional approach, after extracting the ERD/ERS patterns. Comparison of the findings with the ones in the database article (67.46% was reported after using CSP and discarding two subjects) confirms that the ERD/ERS pattern quantification from the O-splines as the best. However, even if the accuracy from the O-splines was higher, the difference between it and the traditional method was not greater than 5 % and can be related to that both methods captured a similar ERD pattern (without considering the high frequency oscillations).

Another possible explanation for this could be the parameter extracted. In this work the mean value of the samples from the para-event time was used, meanwhile in other studies, larger classification accuracies were obtained when using six statistical parameters (86.11 % and 83.24 %) [22] or ERD/ERS differences between electrodes (86.11 %) [23]. Therefore, it is possible that using other parameters from the ERD/ERS patterns from the O-splines could perform better than using only the mean.

The most important result was the classification accuracy obtained after using the O-splines **physical features estimations**, which reached to **92.31 %**. In a quick comparison, this result is at the level of some other previously presented works in section 1.2, where those with higher accuracy are either combinations of techniques for reducing

Table 5.1: Comparison of the best accuracy with O-splines against the best accuracy of other state of the art methods.

State-of-the-art methods comparison		
Method	**Year**	**ACC (%)**
ICA+WT	2021 [44]	99.44
DWT+SPR+CSP	2023 [42]	98.83
Ensemble-EMD	2023 [41]	96.83
Harmony Search	2020 [38]	93.61
CSP+NCA	2020 [30]	~ 93
O-splines	**2023**	**92.31**
Improved-CSP	2019 [32]	91.25
PCC+DWT	2023 [35]	90.88
STFS-CSP	2016 [29]	~ 90.4
DTCWT+NCA+CSP	2022 [37]	89.1

parameters or for de-noising the signal. Table 5.1 illustrates a comparison with other nine of the reviewed methods, where the O-splines was no better than only five of all presented before. However, these data must be interpreted with caution because most of the proposed techniques worked with different databases. Thus, a fairer comparison could be made by using only one database.

These findings suggest that using the O-splines did really extract important information regarding the MI event, although it existed the limitation of some subjects in the datasets that could not induced much of it. Therefore, using these characteristics might be more pertinent than staying with only the traditional approaches' features due that these parameters could complement between each other for better characterization of the event.

5.4 Future Work

Focusing on the first and second activities from this work, the ERD/ERS patterns from the O-splines resulted clearer than those from the traditional method. It has been assumed and further demonstrate, that the influence of the filter design has a major effect

on the estimation. Authors in [54] suggest using among **-54 dB to -60 dB** stop-band attenuation gains in event-related applications, which are larger than the ones marked in the filter of this work. In future investigations, it might be better either to use a higher order filter for extracting band information, or other pre-processing techniques as ICA, WPD or EMD for comparing results with the ones from O-splines.

State estimations' results were encountered using the spectral ROI between 9-13 Hz, as it was the frequency band related to the MI activity from the database recordings. According to literature [18, 3, 42], the frequency band between 8-30 Hz has more representative MI ERD/ERS activity, when alpha and beta bands are combined. Other studies obtained great classification results when using this information instead of only information from one band [22, 42]. Hence, in future investigations, it might be possible to use a different and larger frequency band of interest that covers both alpha and beta bands.

Contrary to the last point, O-splines have also been used as filter bank [64, 62, 83]. Therefore, a proposition is to use this technique as complement with others for extracting the best results. For example, many studies have proposed variations of the CSP method focusing on the filtering step using band-pass filters [53, 26], EMD [50] or wavelets [37, 53, 42]. Thus, extending CSP with O-splines would be a research work to test how the last could support the first method.

Also, these are preliminary results in the MI-EEG analysis field using the O-splines' state estimations. Moreover, there is abundant room for further progress in determining if these parameters could deliver pertinent information about the MI-events. A reduced number of studies considered using amplitude and phase parameters for MI-tasks classification [57, 58, 34]. However, very limited studies used other kind of information related to phase [69]. The O-splines not only gave estimations on these features, but they also estimated frequency and changes of frequency, which have been shown great description results in other studies [60, 68]. Thus, works that take these variables

into account will need to be undertaken in the future with MI-BCI applicability.

5.5   Limitations

Starting with the first activity in this research, the ERD/ERS patterns obtained with the O-splines showed clearer estimations against the traditional method. However, to observe statistical differences, the mean information from the samples inside the MI-event time span (0-3000 ms) was used, leading to similar results between methods. To show differences, another parameter that could better represent the characteristics in time from these patterns could be extracted from the MI-state.

Secondly, the comparison between methods in the first activity of this research was restricted to follow only the ERD/ERS steps from [2]. The difference is that the results in this work used all 52 subjects from the database. A fairer comparison could be to consider only the trials and subjects that the original article took.

Thirdly, the state estimations with the O-splines are limited by the lack of information on applying the different parameters into MI-BCI applications. Amplitude and phase are more commonly used for describing MI-event state [42] and for classification of MI classes [57]. However, derivatives from these characteristics are not normally extracted. Therefore, in this analysis, their results in time were related visually with the previous knowledge in MI.

Chapter 6

Conclusion

The purpose of this thesis work was to examine if the O-splines could be able to characterize MI-EEG patterns by extracting different parameters. This by first comparing them with a traditional approach, such as ERD/ERS: AM, and then, using their state estimation capacity to extract amplitude, phase, frequency, and ROCOF maps of the MI-event.

ERD/ERS analysis via AM approach with both traditional and O-splines methods has resulted in a clearer ERD pattern during MI-event using the last. This result concludes that, generally, the filtering capacity from O-splines outperformed the one from Butterworth. In both cases, the EEG time signal maintained some similarities, but is in the spectral domain that the O-splines demonstrated having a greater effect than Butterworth, as frequencies outside the frequency band of interest were totally cut off from the signal. The evidence from this analysis, presented in Figures 4.3 and 4.4, suggests that Butterworth keeps lower energy from other frequency bands inside the band of interest. Instead, the O-splines keep only the band of interest. This difference could be explained due to the low order the Butterworth filter. With higher order, surely its attenuation capacity would be better. Nevertheless, doing so for this activity would not allow to compare results with the ones from the database validation article.

One of the most significant findings that emerged from the ERD/ERS analysis was that the clearer estimations from the O-splines were captured using all of subjects in the database, instead of only the most significant. Although, the database original article performed a pre-processing step to identify and remove bad subjects from ERD/ERS analysis, considering all of them could give insights about the performance of the technique presented for characterizing the pattern for all people. This last idea is strengthened with the results from the classification process.

This research work has also shown that the O-splines state analysis could extract characteristics related to MI events. Amplitude estimation with O-splines delivered an almost similar behavior encountered in ERD/ERS analysis for both electrodes C3 and C4 during RH- and LH-MI, and its derivatives gave more information from oscillations and energy of the signal. However, non-significant differences between electrodes were found. Spectral features were also obtained with O-splines, but as well as amplitude features, non-significant differences resulted between electrodes. Further analysis could be performed with these characteristics for applying them into a MI classes classification step.

The second major result was the classification accuracies delivered by the different classification models. In the first task, the accuracy obtained with the O-splines was higher than the one from the traditional method, even though the difference was no more than 5%. In the second tasks, the accuracy was higher using the six features extracted from the O-splines. Moreover, this result was compared against nine other state-of-the-art methods, where only five had better performances.

In general, the findings of this research provide insights for the signal processing of MI-EEG signals using the O-splines. It was demonstrated their capacity to quantify the ERD and ERS patterns related to MI-events, and that the state derivatives can also be utilized for analysis of these types of events in a way that all subjects' data are considered. Instead of adapting the data, the method should adapt to the data that is

introduced. In this matter, the O-splines have proven to be a useful technique capable of separating MI activity for all subjects for its characterization.

In addition, future work should be addressed with this technique. Further research might explore other O-splines configurations in MI application, such as using a longer bandwidth or a filter bank. Besides, other traditional and popular methods could be used to compare results with the ones from the O-splines for a more complete conclusion of their capacity on MI application.

Bibliography

[1] G. Pfurtscheller, "Event-related synchronization (ers): An electrophysiological correlate of cortical areas at rest," *Electroencephalography and Clinical Neurophysiology*, vol. 83, pp. 62–69, 1992.

[2] H. Cho, M. Ahn, S. Ahn, M. Kwon, and S. C. Jun, "Eeg datasets for motor imagery brain computer interface," *GigaScience*, vol. 6, no. 7, 2017.

[3] G. Pfurtscheller and F. L. da Silva, "Event-related eeg/meg synchronization and desynchronization: Basic principles," *Clinical Neurophysiology*, vol. 110, pp. 1842–1857, 1999.

[4] P. Clochon, J.-M. Fontbonne, N. Lebrun, and P. Etévenon, "A new method for quantifying eeg event-related desynchronization: Amplitude envelope analysis," *Electroencephalography and Clinical Neurophysiology*, vol. 98, pp. 126–129, 1996.

[5] J. Zhang and M. Wang, "A survey on robots controlled by motor imagery brain-computer interface," *Cognitive Robotics*, vol. 1, 2021.

[6] J. Minguillon, M. A. M. Angel Lopez-Gordo, and F. Pelayo, "Trends in eeg-bci for daily-life: Requirements for artifact removal," *Biomedical Signal Processing and Control*, vol. 31, pp. 407–418, 2017.

[7] A. E. Hramov, V. A. Maksimenko, and A. N. Pisarchik, "Physical principles of brain–computer interfaces and their applications for rehabilitation, robotics and control of human brain states," *Physics Reports*, vol. 918, pp. 1–133, 2021.

[8] P. Lahane, J. Jagtap, A. Inamdar, N. Karne, and R. Dev, "A review of recent trends in eeg based brain-computer interface," in *Second International Coference on Computational Intelligence in Data Science (ICCIDS)*, pp. 1–6, IEEE, 2019.

[9] A. Khosla, P. Khandnor, and T. Chand, "A comparative analysis of signal processing and classification methods for different applications based on eeg signals," *Biocybernetics and Biomedical Engineering*, vol. 40, no. 2, pp. 649–690, 2020.

[10] N. Padfield, J. Zabalza, H. Zhao, V. Masero, and J. Ren, "Eeg-based brain-computer interfaces using motor-imagery: Techniques and challenges," *Sensors*, vol. 19, no. 6, p. 1423, 2019.

[11] C.-T. Lin and T.-T. N. Do, "Direct-sense brain–computer interfacesand wearable computers," *IEEE Transaction on Systems, Man, and Cybernetics: Systems*, vol. 51, no. 1, pp. 298–312, 2021.

[12] M. F. Mridha, S. C. Das, M. M. Kabir, A. A. Lima, M. R. Islam, and Y. Watanobe, "Brain-computer interface: Advancement and challenges," *Sensors*, vol. 21, no. 17, p. 5746, 2021.

[13] M. Jeannerod, *Motor Cognition: What actions Tell the Self*. Lyon, France: Oxford University Press, 2006.

[14] G. Pfurtscheller and A. Aranibar, "Evaluation of event-related desynchronization (erd) preceding and following voluntary self-paced movement," *Electroencephalography and Clinical Neurophysiology*, vol. 46, pp. 138–146, 1979.

[15] G. Pfurtscheller, A. S. Jr, and C. Neuper, "Event-related synchronization (ers) in the alpha band - an electrophysiological correlate of cortical idling: A review," *International Journal of Psychophysiology*, vol. 24, pp. 39–46, 1996.

[16] J. Decety and D. H. Ingvar, "Brain structures participating in mental simulation of motor behavior: A neurpyschological interpretation," *Acta Psychologica*, vol. 73, pp. 13–34, 1990.

[17] R. Beisteiner, P. Höllinger, G. Lindinger, W. Lagn, and A. Berthoz, "Mental representations of movements. brain potentials associated with imagination of hand movements.," *Electroencephalography and Clinical Neurophysiology*, vol. 96, pp. 183–193, 1995.

[18] G. Pfurtscheller and C. Neuper, "Motor imagery activates primary sensorimotor area in humans," *Neuroscience Letters*, vol. 239, no. 2,3, pp. 65–68, 1997.

[19] F. Li, W. Peng, Y. Jiang, L. Song, Y. Liao, C. Yi, L. Zhang, Y. Si, T. Zhang, F. Wang, R. Zhang, Y. Tian, Y. Zhang, D. Yao, and P. Xu, "The dynamic brain networks of motor imagery: Time-varying causality analysis of scalp eeg," *International Journal of Neural Systems*, vol. 28, no. 0, p. 1850016, 2018.

[20] E. Pitsik, N. Frolov, A. Badarin, and V. Grubov, "Network analysis of electrical activity in brain motor cortex during motor execution and motor imagery of elderly," in *2020 International Conference Nonlinearity, Information and Robotics (NIR)*, 2020.

[21] M. Peng, D. Lai, S. Li, Z. Liu, D. Gao, Y. Qin, , and T. Liu, "Effects of brain network segregation and integration on motor imagery sensorimotor rhythm," *Brain-Apparatus Communicaiton: A Journal of Bacomics*, vol. 2, no. 1, p. 2147404, 2023.

[22] N. Bagh and M. R. Reddy, "Hilbert transform-based event-related patterns for motor imagery brain computer interface," *Biomedical Signal Processing and Control*, vol. 62, 2020.

[23] F. Shahlaei, N. Bagh, M. Zambare, and M. R. Reddy, "Quantification of event related brain patterns for the motor imagery tasks using inter-trial variance technique," *Engineering Applications of Artificial Intelligence*, vol. 126, p. 106863, 2023.

[24] S. Chen, X. Shu, J. Jia, H. Wang, L. Ding, Z. He, S. Brauer, and X. Zhu, "Relation between sensorimotor rhythm during motor attempt/imagery and upper-limb motor impairment in stroke," *Clinical EEG and Neuroscience*, vol. 53, pp. 1–10, 2021.

[25] K. Kato, K. Takahashi, N. Mizuguchi, and J. Ushiba, "Online detection of amplitude modulation of motor-related eeg desynchronization using a lock-in amplifier: Comparison with a fast fourier transform, a continuous wavelet transform, and an autoregressive algorithm," *Journal of Neurosciences Methods*, vol. 293, pp. 289–298, 2018.

[26] J. Khan, M. H. Bhatti, U. G. Khan, and R. Iqbal, "Multiclass eeg motor-imagery classification with sub-band common spatial patterns," *EURASIP Journal on Wireless Communications and Networking*, vol. 174, 2019.

[27] C. F. Blanco-Diaz, J. M. Antelis, and A. F. Ruiz-Olaya, "Comparative analysis of spectral and temporal combinations in csp-based methods for decoding hand motor imagery tasks," *Journal of Neuroscience Methods*, vol. 371, p. 109495, 2022.

[28] A. S. Aghaei, M. S. Mahanta, and K. N. Plataniotis, "Separable common spatio-spectral patterns for motor imagery bci systems," *IEEE Transactions on Biomedical Engineering*, vol. 63, no. 1, pp. 15–29, 2016.

[29] M. Miao, H. Zeng, A. Wang, C. Zhao, and F. Liu, "Discriminative spatial-frequency-temporal feature extraction and classification of motor imagery eeg: An sparse regression and weighted naïve bayesian classifier-based approach," *Journal of neuroscience methods*, vol. 278, pp. 13–24, 2016.

[30] M. K. I. Molla, A. A. Shiam, M.-R. Islam, and T. Tanaka, "Discriminative feature selection-based motor imagery classification using eeg signal," *IEEE Access*, vol. 8, pp. 98255–98265, 2020.

[31] S.-H. Park, D. Lee, and S.-G. Lee, "Filter bank regularized common spatial pattern ensemble for small sample motor imagery classification," *IEEE Transactions on Neural Systems and Rehabilitation Engineering*, vol. 26, no. 2, pp. 498–505, 2018.

[32] Z. chuan Tang, C. Li, J. feng Wu, P. cheng Liu, and S. wei Cheng, "Classification of eeg-based single-trial motor imagery tasks using a b-csp method for bci," *Frontiers of Information Technology And Electronic Engineering*, vol. 20, no. 8, pp. 1087–1098, 2019.

[33] W.-Y. Hsu and Y.-W. Cheng, "Eeg-channel-temporal-spectral-attention correlation for motor imagery eeg classification," *IEEE Transactions on Neural Systems and Rehabilitation Engineering*, vol. 31, pp. 1659–1669, 2023.

[34] S. Huang, G. Cai, T. Wang, and T. Ma, "Amplitude-phase information measurement on riemannian manifold for motor imagery-based bci," *IEEE Signal Processing Letters*, vol. 28, 2021.

[35] R. D. Pawan, "Electroencephalogram channel selection based on pearson correlation coefficient for motor imagery-brain-computer interface," *Measurement: Sensors*, vol. 25, p. 100616, 2023.

[36] Y. You, W. Chen, and T. Zhang, "Motor imagery eeg classification based on flexible analytic wavelet transform," *Biomedical Signal Processing and Control*, vol. 62, 2020.

[37] N. S. Malan and S. Sharma, "Motor imagery eeg spectral-spatial feature optimization using dual-tree complex wavelet and neighbourhood component analysis," *IRBM*, vol. 43, no. 3, pp. 198–209., 2022.

[38] S. Mohdiwale, M. Sahu, G. Sinha, and V. Bhateja, "Statistical wavelets with harmony search based optimal feature selection of eeg signals for motor imagery classification," *IEEE Sensors Journal*, vol. 21, no. 13, pp. 14263–14271, 2020.

[39] J. Jin, C. Liu, I. Daly, Y. Miao, S. Li, X. Wang, and A. Cichocki, "Bispectrum-based channel selection for motor imagery based brain-computer interfacing," *IEEE Transactions on Neural Systems and Rehabilitation Engineering*, vol. 28, no. 10, pp. 2153–2163, 2020.

[40] M. Ortiz, M. Rodriguez-Ugarte, E. Iáñez, and J. Azorín, "Comparison of different eeg signal analysis techniques for an offline lower limb motor imagery brain-computer interface," in *2018 40th Annual International Conference of the IEEE Engineering in Medicine and Biology Society (EMBC)*, pp. 203–206, IEEE, 2018.

[41] V. S. Kardam, S. Taran, and A. Pandey, "Motor imagery tasks based electroencephalogram signals classification using data-driven features," *Neuroscience Informatics*, vol. 3, p. 100128, 2023.

[42] N. Bagh and M. R. Reddy, "Investigation of the dynamical behavior of brain activities during rest and motor imagery movements," *Biomedical Signal Processing and Control*, vol. 79, p. 104153, 2023.

[43] X. Geng, D. Li, H. Chen, P. Yu, H. Yan, and M. Yue, "An improved feature extraction algorithms of eeg signals based on motor imagery brain-computer interface," *Alexandria Engineering Journal*, vol. 61, pp. 4807—-4820, 2022.

[44] N. K. Al-Qazzaz, Z. A. A. Alyasseri, K. H. Abdulkareem, N. S. Ali, M. N. Al-Mhiqani, and C. Guger, "Eeg feature fusion for motor imagery: A new robust framework towards stroke patients rehabilition," *Computers in Biology and Medicine*, vol. 137, p. 104799, 2021.

[45] L. Hu, "Single-trial analysis," in *EEG Signal Processing and Feature Extraction* (L. Hu and Z. Zhang, eds.), pp. 89–116, Singapore: Springer, 2019.

[46] J. Müller-Gerking, G. Pfurtscheller, and H. Flyvbjerg, "Designing optimal spatial filters for single-trial eeg classifcation in a movement task," *Clinical Neurophysiology*, vol. 110, pp. 787–798, 1999.

[47] L. Cheng, D. Li, X. Li, and S. Yu, "The optimal wavelet basis function selection in feature extraction of motor imagery electroencephalogram based on wavelet packet transformation," *IEEE Access*, vol. 7, pp. 174465–174481, 2019.

[48] J. Meng and B. He, "Exploring trainning effect in 42 human subjects using a non-invasive sensorimotor rhythm based online bci," *Frontier in Human Neuroscience*, vol. 13, no. 128, 2019.

[49] S. Aggarwal and N. Chugh, "Signal processing techniques for motor imagery brain computer interface: A review," *Array*, vol. 1, no. 2, p. 100003, 2019.

[50] P. Gaur, R. B. Pachori, H. Wang, and G. Prasad, "An automatic subject specific intrinsic mode function selection for enhancing two-class eeg based motor imagery-brain computer interface," *IEEE Sensors Journal*, vol. 19, no. 16, pp. 6938–6947, 2019.

[51] S. Liang, K.-S. Choi, J. Qin, W.-M. Pang, and P.-A. Heng, "Classificatoin of motor imageru tasks using phase synchronization of eeg based on multivariate empirical mode decomposition," in *2014 4th IEEE International Conference on Information Science and Technology*, pp. 674–677, IEEE, 2014.

[52] T.-C. Wang, Y.-Y. Huang, and J.-R. Duann, "Sources of independent mu component reveal different brain areas involved in motor imagery, motor execution, and movement observation," *Brain Research*, vol. 1796, p. 148075, 2022.

[53] P. Rithwik, V. K. Benzy, and A. P. Vinod, "High accuracy decoding of motor imagery directions from eeg-based brain computer interface using filter bank spatially regularised common spatial pattern method," *Biomedical Signal Processing and Control*, vol. 72, p. 103241, 2022.

[54] A. Widmann, E. Schroger, and B. Maess, "Digital filter design for electrophysiological data – a practical approach," *Journal of Neuroscience Methods*, vol. 250, pp. 34–46, 2015.

[55] A. de Cheveigné and I. Nelken, "Filters: When, why, and how (not) to use them," *Neuron*, vol. 102, no. 2, pp. 280–293, 2019.

[56] V. Gonuguntla, Y. Wang, and C. Veluvolu, "Phase synchrony in subject-specific reactive band of eeg for classification of motor imagery tasks," in *35th Annual International Conference of the IEEE EMBS*, 2013.

[57] M. Bhatnagar, G. S. Gupta, and R. K. Sinha, "k-nn and lda based motor imagery eeg classification using phase features," in *2018 5th IEEE Uttar Pradesh Section International Conference on Electrical, Electronics and Computer Engineering (UPCON)*, pp. 1–6, IEEE, 2018.

[58] B. Xu, Z. Wei, A. Song, C. Wu, D. Zhang, W. Li, G. Xu, H. Li, and H. Zeng, "Phase synchronization information for classifying motor imagery eeg from the same limb," *IEEE Access*, vol. 7, pp. 153842–153852, 2019.

[59] B. VK and A. Vinod, "Classification of motor imagery hand movement directions from eeg extracted phase locking value features for brain computer interfaces," in *TENCON 2019-2019 IEEE Region 10 Conference (TENCON)*, pp. 2315–2319, IEEE, 2019.

[60] J. A. de la O Serna, "Analyzing power oscillating signals with the o-splines of the discrete taylor-fourier transform," *IEEE Transactions on Power Systems*, vol. 33, no. 6, pp. 7087–7095, 2018.

[61] M. A. Plata-Garza and J. A. de la O Serna, "Dynamic harmonic analysis through taylor-fourier transform," *IEEE Transactions on Instrumentation and Measurement*, vol. 60, no. 3, pp. 804–813, 2011.

[62] J. A. de la O Serna, Mario, R. A. Paternina, A. Zamora-Mendez, R. K. Tripathy, and R. B. Pachori, "Eeg-rhythm specific taylor-fourier filter bank implemented with o-splines for the detection of epilepsy using eeg signals," *IEEE Sensors Journal*, vol. 20, no. 12, pp. 6542–6551, 2020.

[63] J. A. de la O Serna, Mario, R. A. Paternina, and A. Zamora-Mendez, "Assessing synchrophasor estimates of an event captured by a phasor measurement unit," *IEEE Transactions on Power Delivery*, vol. 36, no. 5, pp. 3109–3117, 2020.

[64] D. Guillen, J. A. de la O Serna, M. A. Zamora-Mendez, R. A. Paternina, and F. Salinas, "Taylor-fourier filter bank implemented with o-splines for the detection and classification of faults," *IEEE Transactions on Industrial Informatics*, vol. 17, no. 5, pp. 3079–3089, 2020.

[65] D. Rodales, A. Zamora-Mendez, J. A. de la O Serna, J. M. Ramirez, M. R. A. Paternina, L. Lugnani, G. E. Mejia-Ruiz, A. Sanchez-Ocampo, and D. Dotta, "Model-free inertia estimation in bulk power grids through o-splines," *International Journal of Electrcal Power and Energy Systems*, vol. 153, p. 109323, 2023.

[66] J. A. de la O Serna, "Taylor-fourier analysis of blood pressure oscillometric waveforms," *IEEE Transactions on Instrumentation and Measurement*, vol. 62, no. 9, pp. 2511–2518, 2013.

[67] R. K. Tripathy, A. Zamora-Mendez, J. A. de la O Serna, M. R. A. Paternina, J. G. Arrieta, and G. R. Naik, "Detection of life threatening ventricular arrhythmia using digital taylor-fourier transform," *Frontiers in Physiology*, vol. 9, 2018.

[68] J. A. de la O Serna, "Dynamic harmonic analysis with fir filters designed with o-splines," *IEEE Transactions on Circuits and Systems I: Regular Papers*, vol. 67, no. 12, pp. 5092–5100, 2020.

[69] S.-B. Lee, H.-J. Kim, H. Kim, J.-H. Jeong, S.-W. Lee, and D.-J. Kim, "Comparative analysis of features extracted from eeg spatial, spectral and temporal domains for binary and multiclass motor imagery classification," *Information Science*, vol. 502, pp. 190–200, 2019.

[70] Z. Zhang, "Spectral and time-frequency analysis," in *EEG Signal Processing and Feature Extraction* (L. Hu and Z. Zhang, eds.), pp. 89–116, Singapore: Springer, 2019.

[71] D. Jaipriya and K. C. Sriharipriya, "Brain computer interface-based signal processing techniques for feature extraction and classification of motor imagery using eeg: A literature review," *Biomedical Materials And Devices*, pp. 1–13, 2023.

[72] A. Sovic and D. Sersic, "Signal decompositino methods for reducing drawbacks of the dwt," *Engineering Review*, vol. 32, no. 2, pp. 70–77, 2012.

[73] J. G. Proakis and M. Salehi, *Digital Communications*, ch. 2, pp. 17–94. McGrraw-Hill Higher Education, 2008.

[74] M. Feldman, "Hilbert transform in vibration analysis," *Mechanical Systems and Signal Processing*, vol. 25, pp. 735–802, 2011.

[75] D. Manolakis and V. Ingle, *Applied Digital Signal Processing, Theory and Practice*, ch. 7. New York, USA: Cambridge University Press, 2011.

[76] J. A. de la O Serna, "Dynamic phasor estimates for power system oscillations," *IEEE Transactions on Instrumentation and Measurement*, vol. 56, no. 5, pp. 1648–1657, 2007.

[77] C.-Y. Kee, S. G. Ponnambalam, and C.-K. Loo, "Binary and multi-class motor imagery using renyi entropy for feature extraction," *Neural Computing and Application Forum 2016*, vol. 28, pp. 2051–2062, 2017.

[78] Y. Zhang, C. S. Nam, X. W. Guoxu Zhou, and A. Cichocki, "Temporally constrained sparse group spatial patterns for motor imagery bci," *IEEE Transactions on Cybernetics*, vol. 49, no. 9, pp. 3322–3332, 2018.

[79] D. J. McFarland, L. M. McCane, S. V. David, and J. R. Wolpaw, "Spatial filter selection for eeg-based communication," *Electroencephalography and Clinical Neurophysiology*, vol. 103, pp. 386–394, 1997.

[80] M. Kwon, H. Cho, K. Won, M. Ahn, and S. C. Jun, "Event-related desynchronization (erd) may not be correlated with motor imagery bci performance," in *2018 IEEE International Conference on Systems, Man, and Cybernetics*, IEEE, 2018.

[81] C. Linding-Leon and L. Bougrain, "Comparison of sensorimotor rhythms in eeg signals during simple and combined motor imageries over the contra and ipsilateral hemispheres," in *2015 37th Annual International Conference of the IEEE Engineering in Medicine and Biology Society (EMBC)*, IEEE, 2015.

[82] B. Grainmann and G. Pfurtscheller, *Quantification and Visualization of Event-Related Changes in Oscillatory Brain Activity in the Time-Frequency Domain*, ch. 6, pp. 79–97. Progress in Brain Research, 2006.

[83] R. K. Tripathy, J. A. de la O Serna, A. Zamora-Mendez, M. R. A. Paternina, H. R. Chamorro, P. Koutakis, and C. Konstantinou, "O-splines implemented taylor-fourier filter-bank for the elimination of artifacts from ppg signals," *IEEE Access*, unpublished.

[84] Z. Zhou and B. Wan, "Wavelet packet-based independent component analysis for feature extraction from motor imagery eeg of complex movements," *Clinical Neurophysiology*, vol. 123, pp. 1779–1788, 2012.

[85] A. Delorme and S. Makeig, "Eeglab: An open source toolbox for analysis of single-trial eeg dynamics including independent component analysis," *Journal of Neuroscience Methods*, vol. 134, pp. 9–21, 2004.

[86] S. I. Alzahrani and M. M. Alsaleh, "The influence of smoothing filtering methods on the performance of an eeg-based brain–computer interface," *IEEE Access*, vol. 11, pp. 60171–60180, 2023.

[87] L. Yakovlev, N. Syrov, A. Miroshnikov, M. Lebedev, and A. Kaplan, "Event-related desynchronization induced by tactile imagery: an eeg study," *Sensory and Motor Systems*, vol. 10, no. 6, pp. 1–12, 2023.

Appendix A

State estimators

A.1 Analytic Signal

$$x(t) = a(t)cos\phi(t) = \xi(t) + \xi^*(t) \tag{A.1}$$

where

$$\xi(t) = \frac{1}{2}a(t)e^{j\phi(t)} \tag{A.2}$$

where $2\xi(t)$ is the analytic signal. When $\phi(t) = \omega_1 t + \varphi(t)$, then we have

$$\xi(t) = \frac{1}{2}a(t)e^{j\varphi(t)}e^{j\omega_1 t} = \psi(t)e^{j\omega_1 t} \tag{A.3}$$

with $\psi(t)$ the dynamic phasor, with

$$\psi(t) = \xi(t)e^{-j\omega_1 t} \tag{A.4}$$

From these equations we have

$$a(t) = |2\xi(t)| \qquad \phi(t) = \angle\xi(t) \qquad \varphi(t) = \angle\psi(t) \tag{A.5}$$

A.2 First Derivative

$$\dot{x}(t) = \dot{a}(t)cos\phi(t) - a(t)\dot{\phi}(t)sin\phi(t) \tag{A.6}$$

$$\dot{\xi}(t) = \frac{1}{2}[\dot{a}(t) + ja(t)\dot{\phi}(t)]e^{j\phi(t)} \tag{A.7}$$

$$\dot{\psi}(t) = [\dot{\xi}(t) - j\xi(t)\omega_1]e^{-j\omega_1 t} = \frac{1}{2}[\dot{a}(t) + ja(t)\dot{\phi}(t)]e^{j\varphi(t)} \tag{A.8}$$

$$\dot{a}(t) = \Re\{2\dot{\xi}(t)e^{-j\phi(t)}\} \qquad \dot{\phi}(t) = \Im\{2\dot{\xi}(t)e^{-j\phi(t)}\}/a(t) \tag{A.9}$$

$$\dot{a}(t) = \Re\{2\dot{\psi}(t)e^{-j\varphi(t)}\} \qquad \dot{\varphi}(t) = \Im\{2\dot{\psi}(t)e^{-j\varphi(t)}\}/a(t) \tag{A.10}$$

A.3 Second Derivative

$$\ddot{x}(t) = [\ddot{a}(t) - a(t)\dot{\phi}(t)^2]cos\phi(t) - [2\dot{a}(t)\dot{\phi}(t) + a(t)\ddot{\phi}(t)]sin\phi(t) \tag{A.11}$$

$$\ddot{\xi}(t) = \frac{1}{2}[(\ddot{a}(t) - a(t)\dot{\phi}(t)^2) + j(2\dot{a}(t)\dot{\phi}(t) + a(t)\ddot{\phi}(t))]e^{j\phi(t)} \tag{A.12}$$

$$\ddot{\psi}(t) = [(\ddot{\xi}(t) - \omega_1^2\xi(t)) - j2\omega_1\dot{\xi}(t)]e^{-j\omega_1 t} \tag{A.13}$$

$$= \frac{1}{2}[\ddot{a}(t) - a(t)\dot{\varphi}(t)^2 + j(2\dot{a}(t)\dot{\varphi}(t) + a(t)\ddot{\varphi}(t))]e^{j\varphi t} \tag{A.14}$$

From these equations, we have in terms of the absolute phase $\phi(t)$:

$$\ddot{a}(t) = \Re\{2\ddot{\xi}(t)e^{-j\phi(t)}\} + a(t)\dot{\phi}(t)^2$$

$$\ddot{\phi}(t) = [\Im\{2\ddot{\xi}(t)e^{-j\phi(t)}\} - 2\dot{a}(t)\dot{\phi}(t)]/a(t) \tag{A.15}$$

or in terms of the relative phase $\varphi(t)$:

$$\ddot{a}(t) = \Re\{2\ddot{\psi}(t)e^{-j\varphi(t)}\} + a(t)\dot{\varphi}(t)^2$$

$$\ddot{\varphi}(t) = [\Im\{2\dot{\psi}(t)e^{-j\varphi(t)}\} - 2\dot{a}(t)\dot{\varphi}(t)]/a(t)$$

(A.16)